DISSERTATION

Effect of local and global connectivity of phases on damage evolution in cast Al-Si alloys

carried out for the purpose of obtaining the degree of Doctor technicae (Dr. techn.), submitted at TU Wien, Faculty of Mechanical and Industrial Engineering, by

Katrin BUGELNIG

Matr.Nr.: 0626171

under the supervision of

Univ.Prof. Dr. techn. Guillermo Carlos Requena

Department of Metallic Structures and Hybrid Materials Systems, German Aerospace Centre (DLR), Linder Höhe, 51147 Cologne, Germany

Metallic Structures and Materials Systems for Aerospace Engineering, RWTH Aachen University, 52062 Aachen, Germany

reviewed by

assoc. Prof. Dr.mont.   Ao. Univ. Prof. Dr.techn.

Stefan Pogatscher   Christian Edtmaier

Chair of Nonferrous Metallurgy,   Institute of Chemical Technologies

Montanuniversitaet Leoben   and Analytics, TU Wien

Erzherzog-Johann-Straße 3/II,   Getreidemarkt 9,

A-8700 Leoben   A-1060 Wien

I confirm that going to press of this thesis needs the confirmation of the examination committee.

Affidavit

I declare in lieu of oath, that I wrote this thesis and performed the associated research myself, using only literature cited in this volume. If text passages from sources are used literally, they are marked as such.

I confirm that this work is original and has not been submitted elsewhere for any examination, nor is it currently under consideration for a thesis elsewhere.

Vienna, August, 2019

_____

Signature

ACKNOWLEDGEMENTS

KURZFASSUNG

Neben Ti- und Mg-Legierungen, gewinnen Al-Legierungen auf Grund ihrer Kosteneffizenz, Leichtigkeit und exzellenten thermischen und mechanischen Eigenschaften zunehmend an Bedeutung. Insbesondere Al-Si Gussteile werden immer öfter für Kolbenanwendungen in der Automobilindustrie gewählt. Jedoch führt die steigende Nachfrage nach leistungsfähigeren Verbrennungsmotoren, vorangetrieben durch Umweltvorschriften, zu thermo-mechanischen Zuständen, die an den Grenzen der Belastbarkeit konventioneller Al-Si Kolbenlegierungen liegen. Eine Optimierung hin zu verbesserter Hochtemperaturfestigkeit bei ausreichender Raumtemperatur-duktilität ist daher unbedingt nötig. Die Leistung von Al-Si Kolbenlegierungen ist stark abhängig von ihrer inneren Architektur bestehend aus 3D Netzwerken aus Si und intermetallischen Phasen, die in eine ausscheidungshärtbare α-Al Matrix eingebettet sind.

In dieser Arbeit, bestehend aus drei begutachteten Veröffentlichungen, wurde die Korrelation zwischen Mikrostruktur und Schädigungsentwicklung ausgewählter gegossener, nah-eutektischer Al-Si Kolbenlegierungen als Funktion der chemischen Zusammensetzung und Wärmebehandlung untersucht. 2D und in-situ 3D bildgebende Methoden dienten zur Identifizierung mikrostruktureller Features, die den Prozess der Schädigungsentstehung und –akkumulation während der Zugverformung bei Raumtemperatur (RT) und erhöhten Temperaturen beeinflussen.

In der ersten Publikation wurde der Effekt der 3D Konnektivität des Netzwerkes der rigiden Phasen auf die Schädigungsentwicklung während Zugverformung bei RT als Funktion des Lösungsglühens (ST) untersucht. Während des Lösungsglühens bei 500°C für 4 Stunden, zeigte eine gegossene AlSi12Cu4Ni2 Legierung einen Verlust an *lokaler Konnektivität* (quantifiziert durch den topologischen Parameter Euler-Zahl, χ) bei gleichbleibender *globaler Interkonnektivität* und Matrixhärte auf Grund der partiellen Auflösung und morphologischen Änderungen von Al$_2$Cu Aluminiden als auch leichter Einformung und Fragmentierung von eutektischem und primärem Si. Zugversuche bei Raumtemperatur zeigten im 0h ST Zustand höhere Festigkeit und geringere Duktilität als im 4h ST Zustand. In situ Synchrotron Tomographie (sXCT) während der Zugversuche zeigte keine Änderung in Schädigungsmechanismen

abhängig von der Lösungsglühzeit. Schädigung entsteht hauptsächlich in Verbindung mit Mikrorissen an primären Si in Clustern. Beim Versagen propagiert der Hauptriss ausschließlich entlang entstandener Schädigung und rigider Phasen. Der Verlust an lokaler Konnektivität durch das ST führt zu einem Verlust an Lastaufnahmekapazität des hybriden 3D Netzwerkes und somit zu reduzierter Festigkeit. Gleichzeitig erlaubt dieser, mehr Schädigung und plastischer Dehnung aufzunehmen, was in einer Steigerung der Bruchdehnung der Legierung im 4h ST Zustand resultiert.

Die zweite Publikation beschäftigt sich mit dem Effekt der lokalen Konnektivität des rigiden Netzwerks auf die Festigkeit während Zugverformung bei erhöhten Temperaturen als Funktion der chemischen Zusammensetzung. Eine Erhöhung um 1 wt.% Ni in gegossenen AlSi12Cu4Ni(2,3)Mg Legierungen führt, auf Grund der zusätzlichen Bildung Nadel-artiger Al-Ni-Cu-reicher δ-Phase, zu einer Steigerung der *lokalen Konnektivität* des hybriden Netzwerks um ~40% bei konstanter *globaler Interkonnektivität* und Matrixhärte. In-situ sXCT während Zugversuchen bei 300°C zeigte, dass, im Gegensatz zu RT Beobachtungen, Schädigung nicht nur an primären Si Clustern, sondern auch an Netzwerk/Matrix-Schnittstellen und in der Matrix entsteht. Der Hauptriss propagiert auch durch die Al-Matrix. Die Legierung mit nur 2 wt.% Ni zeigte 10% höhere Festigkeit und ~30% höhere Bruchdehnung im Vergleich zur 3 wt.% Ni Legierung. Dies kann der niedrigeren lokalen Konnektivität ihres rigiden Netzwerks zugeschrieben werden, die eine lokalisierte Plastifizierung der Matrix erlaubt und hilft, vor dem Versagen mehr Schädigung aufzunehmen. Ein analytischer Lastverteilungsansatz, der die Entwicklung der lokalen Konnektivität von rigiden Netzwerken als Funktion der Dehnung mitberücksichtigt, wird basierend auf experimentellen in-situ Daten vorgeschlagen.

In der dritten Publikation wurde eine optimierte Segmentierungsmethode mit Fokus auf akkuratere Evaluierung der lokalen Konnektivität über große, repräsentative Volumen entwickelt. Eine Kombination von konventioneller Röntgentomographie (XCT), sXCT und chemischem Tiefenätzen + Tomographie derselben Legierung an derselben Stelle ermöglicht eine direkte Segmentierung durch einfaches globales Grauwert-Thresholding und genauere Charakterisierung von Phasen als auch Phasen-Schnittstellen über große, repräsentative Volumen und liefert somit die für die Quanti-fizierung benötigten Informationen der gesamten 3D Mikrostruktur der Legierungen.

ABSTRACT

Besides Ti- and Mg-alloys, Al-alloys are continuously gaining in significance as a low cost, light weight material with excellent thermal and mechanical properties. Especially Al-Si castings are a favorable choice for automotive piston applications. However, the rising demand for more efficient combustion engines, pushed by environmental regulations, leads to thermo-mechanical conditions at the limits of operability of conventional cast Al-Si piston alloys, especially at the bowl rim area facing towards the combustion chamber. It is thus imperative to optimize Al-Si piston alloys towards better high temperature strength at sufficient ambient temperature ductility for improved operability. The performance of Al-Si piston alloys is strongly dependent on their internal architecture consisting of hybrid 3D networks formed by Si and intermetallic phases embedded in a precipitation hardened α-Al matrix.

This work comprises three peer-reviewed publications that deal with the correlation between microstructure and damage evolution of selected cast, near eutectic Al-Si piston alloys as a function of chemical composition and heat treatment. 2D and in-situ 3D imaging methods were used to identify microstructural features affecting the processes of damage formation and accumulation during tensile deformation at ambient and elevated temperatures.

In the first publication the effect of 3D connectivity of rigid phase networks on damage formation and accumulation during room temperature tensile deformation was investigated as a function of solution treatment (ST). After 4 hours at 500°C , a cast AlSi12Cu4Ni2 alloy experiences a loss of *local connectivity* (quantified by the topological parameter Euler number, χ) at constant *global interconnectivity* and matrix hardness owing to the partial dissolution and morphological changes of Al_2Cu aluminides as well as slight spheroidization and fragmentation of eutectic and primary Si. Tensile tests at room temperature (RT) reveal higher strength and lower ductility for the as cast condition compared to the 4h ST condition. In situ Synchrotron tomography (sXCT) during tensile deformation revealed no change in damage mechanisms depending on ST time. Damage initiation is mainly associated to micro-cracking through primary Si particles grouped in clusters. At fracture, the main crack exclusively propagates along earlier microcracks formed at rigid phases. The loss of

local connectivity of the 4h ST condition contributes to the loss of load carrying capacity of the 3D hybrid network und thus, results in reduced strength. This also allows the solution treated alloy to accommodate more damage and plastic strain, increasing its elongation at fracture with respect to the as cast condition.

The second publication deals with the effect of local connectivity of 3D hybrid networks on strength during elevated temperature tensile deformation as a function of chemical composition. An increase of 1 wt.% Ni in cast AlSi12Cu4Ni(2,3)Mg alloys leads to an increase of *local connectivity* by ~40%, at constant *global interconnectivity* of rigid 3D hybrid network and matrix hardness owing to the formation of an additional needle-like Al-Ni-Cu-rich δ-phase. In-situ sXCT during tensile deformation at 300°C shows, in contrary to RT observations, damage formation not only through primary Si particles grouped in clusters, but also voids at matrix/rigid phase interfaces as well as in the matrix. The main crack also propagates through the matrix. The alloy with only 2 wt.% Ni exhibits 10% higher strength and ~30% larger elongation at fracture compared to the 3 wt.% Ni alloy. This is attributed to the lower local connectivity of its hybrid 3D network which permits localized plastification of the matrix and helps accommodating more damage prior to failure. A simple analytical load partition approach that considers the evolution of local connectivity of rigid networks as a function of strain is proposed based on in-situ experimental data.

Finally, in the third publication, an optimized segmentation method was developed for an accurate evaluation of local connectivity over large, representative volumes. A combination of laboratory x-ray tomography (XCT), sXCT and deep etching + tomography performed on the same specimen and at the same position allows for direct segmentation using simple global grey value thresholding and a more accurate characterization of phases as well as rigid phase interfaces across large representative volumes and thus provides the information necessary for a quantification of the whole 3D microstructure of the alloys.

TABLE OF CONTENTS

INTRODUCTION & MOTIVATION

The rising demand for more efficient combustion engines, pushed by environmental regulations, calls for the continuous optimization of engine parts and materials used for their production [1]. Besides restrictions regarding pollutant emission, another demand is the reduction of emission of the greenhouse gas CO_2, which is directly correlated to fuel consumption. An efficient measure to reduce consumption is to increase the mean pressure allowing to decrease the engines cubic capacity at constant effective performance. With this downsizing, specific output will increase and so will complex thermo-mechanical loading on engine components (see Fig. 1) [2].
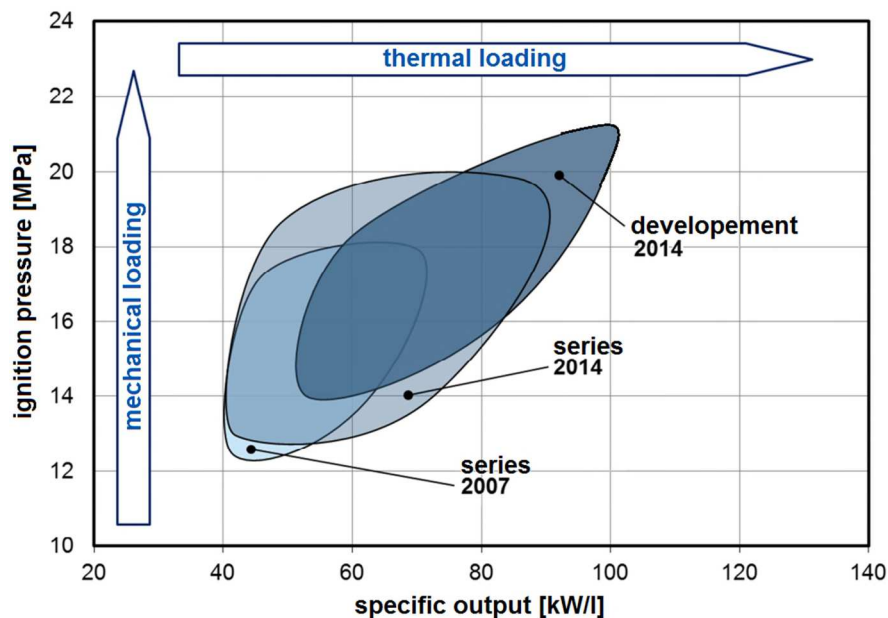
Fig. 1. Evolution of ignition pressure and specific output over the past view years [2].

Pistons have to be able to withstand harsh operation-conditions such as high temperature and pressure, complex friction and superimposed thermo-mechanical loading [3,4]. They are a part of the internal combustion engine with no possibility for maintenance and hence, limit the lifetime of the entire engine [5]. Generally, the bowl rim area, facing the combustion chamber, is the lifetime determining factor for pistons. Owing to the combination of ignition pressure and exposure to temperatures up to 400°C (see Fig. 2 (a)) [2-4], this part experiences demanding thermo-mechanical loading conditions. Mechanical loading is induced by alternating bending around the piston pin under gas, while thermal loading is induced by thermal cycles of

a few seconds caused by alternate temperature-loading with low frequencies as it is the case for the change from idle-running to full-throttle motor conditions [2]. With sufficiently high temperature gradient, the induced stresses can result in plastic deformation (see Fig. 2 (b)). Thus, the for piston applications selected material is required to exhibit extraordinary thermo-mechanical stability.
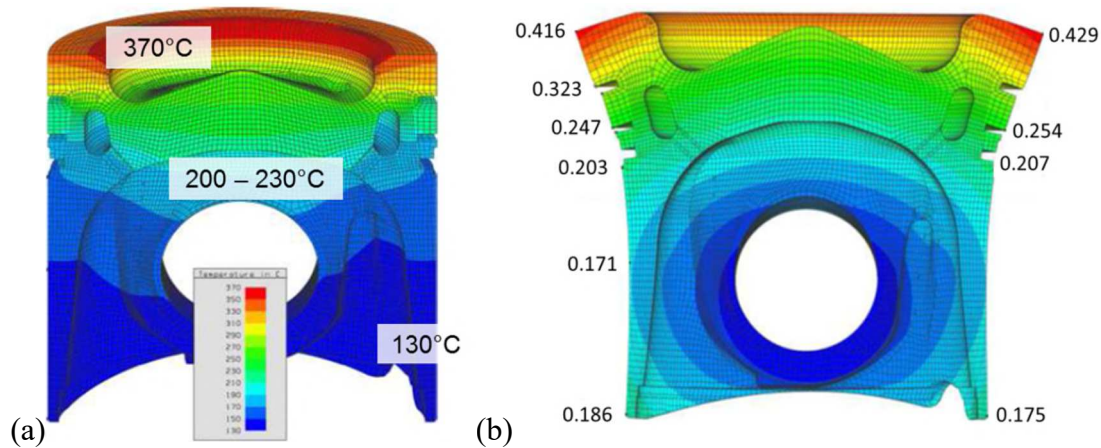
Fig. 2. (a) temperature distribution during engine full throttle, (b) plastic deformation (in [mm]) of the piston owing to thermo-mechanical loading [3].

Moreover, the formation of complex tensile and compressive stress conditions over wide temperature ranges during operation can lead to the formation of fatigue micro-cracks that can rapidly propagate. Thus, sufficient ductility at lower temperatures must also be retained to avoid premature failure of the piston (see Fig. 3) [4-6].
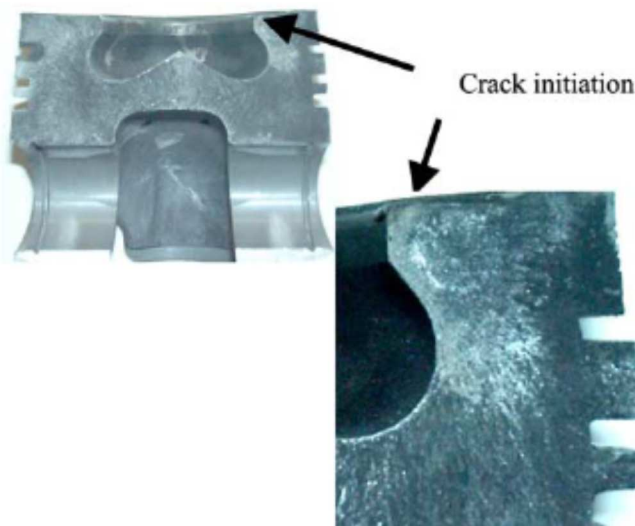
Fig. 3. Premature failure of a diesel piston owing to fatigue cracking originating from the bowl rim area near the combustion chamber [4].

Al based alloys are frequently used for piston applications. In order to fulfill the requirements, pistons have to work efficiently even while being subjected to high thermal and mechanical loadings, without losing the lightweight advantage and recyclability provided by Al alloys [7]. In this context, cast near-eutectic Al-Si alloys have been widely employed in piston applications working at ambient and elevated temperature owing to excellent characteristics such as light weight, low cost manufacturing, excellent castability, wear resistance, low thermal expansion, high specific strength and recyclability [6,8-10].

Chapter 2

STATE OF THE ART

2.1. Cast Al-Si alloys

For automotive engine applications, cast Al-Si alloys present an attractive alternative to steel products owing to their relatively high strength-to-weight ratio, excellent castability, thermal conductivity, good processability, corrosion resistance and cost effectiveness [2,6,10].

2.1.1. Microstructure of cast Al-Si alloys

The eutectic point of the binary Al-Si system can be found at 577°C with Si contents of ~12.6 wt.% (see Fig. 4) [11,12]. Cast Al-alloys containing Si contents > 7 wt.% typically lead to the formation of highly interconnected 3D eutectic Si networks embedded in the interdendritic region [13-15]. Representative microstructures of cast binary Al-Si alloys with typical eutectic and primary Si phase morphologies are shown in Fig. 4 for hypoeutectic and hypereutectic alloys. Since the solubility of Al in Si is very low, the Si phase basically consists of pure silicon [12].
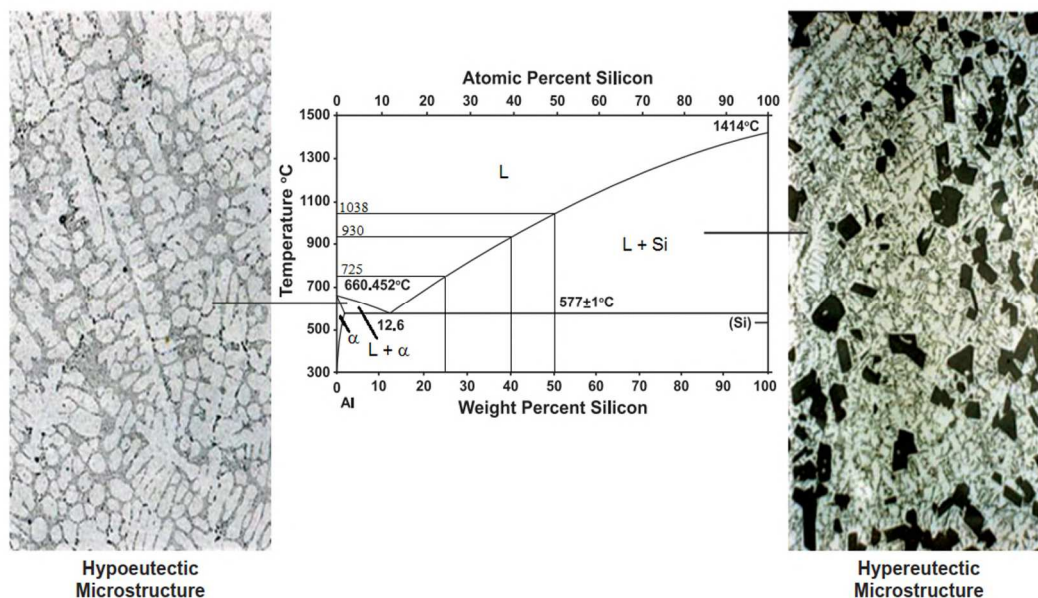
Fig. 4. Binary Al-Si phase diagram with representative microstructures for (left) a hypoeutectic alloy (Si ≤ 12 wt.%) and (right) a hypereutectic alloy (Si > 12 wt.%) [11].

Katrin Bugelnig

3

2.1.1.1. Eutectic Si phase

In general, there are two ways to influence the size and morphology of eutectic Si during solidification: (1) changes in solidification rate during casting (quench - modification) [9,16,-19] and (2) changes in chemical composition by addition of modifiers such as Sr, Na, Ca, Ti or Sb [16,18,19].

Solidification rate (quench modification)

The solidification rate has a significant effect on the size- and morphology-distribution and composition of microstructural constituents [19,20].
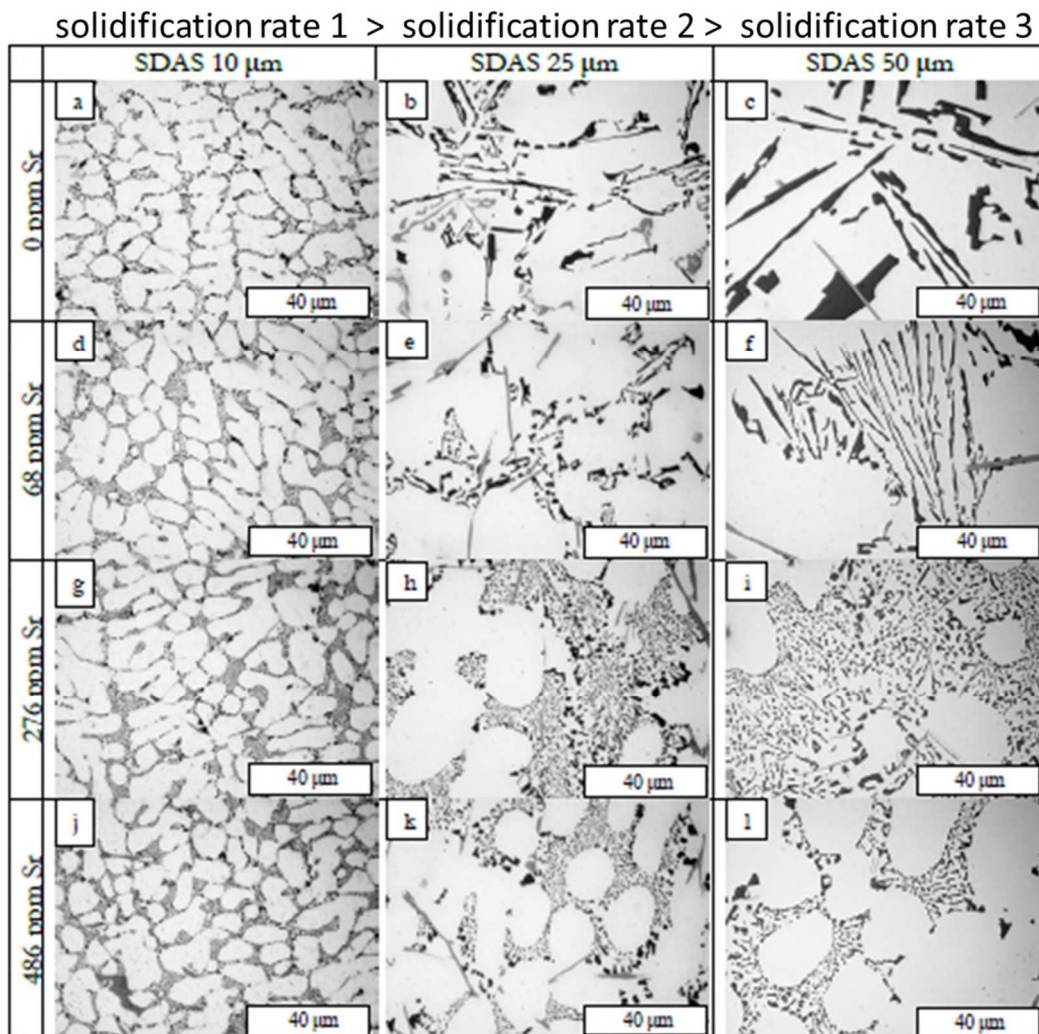
Fig. 5. Microstructure refinement and Si morphology as a function of solidification rate and Sr content in a directionally solidified AlSi8Cu2Mg0.3FeZnMn0.2 alloy [19].

One of the most widely accepted theories on quench modification is based on the surface energy of the Al-Si solid interface [20]. Due to the large difference in thermal conductivity of pure Al and Si and the difference in their latent heat of fusion, Al will

solidify faster than Si. An increase in cooling rate will allow Al to completely encase the far more slowly solidifying Si and thus, hinder its growth.

Although quench modification was found to have significant impact on the coarseness of eutectic Si, no particular changes in Si structure in regards to twin density could be observed (see Fig. 5) [19,21]. However, the usability of quench modification in industrial applications is limited by the achievable cooling rates during conventional casting processes [11].

Chemical modification

While elements such as Ti, B, Zr and V are used to refine α-Al grains (e.g. [22,23]), modifiers of Al alloys such as Sr, Sb, Na, Ba and Ca are used to change the size and morphology of eutectic Si. Because of its easiness in handling, its effectiveness and its low fading effect, Sr is one of the most frequently used modifier elements. The addition of Sr provokes morphological changes of the eutectic Si from coarse flakes to fine fibrous morphologies (see Fig. 6) [16,18]. There are currently several theories explaining the mechanism of modification of eutectic Si provoked by Sr including the consideration of changes in the nucleation or growth levels [24], such as the impurity-included twinning (ITT) [21] and the twin-plane re-entrant edge (TPRE) poising mechanisms [25].
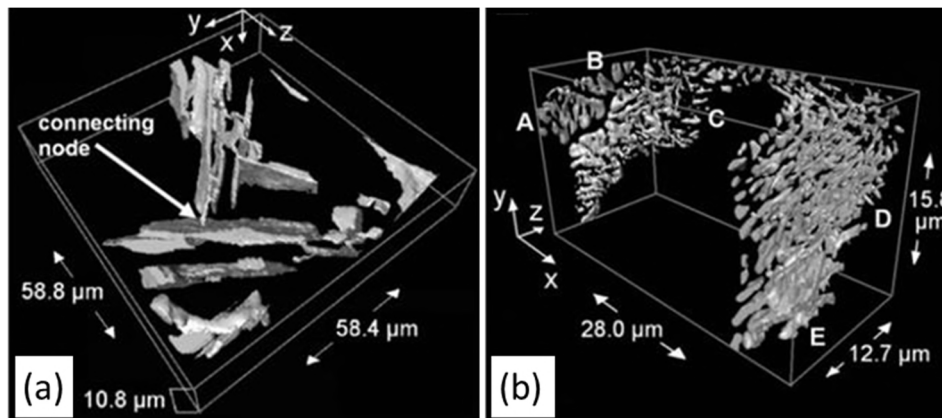
Fig. 6. 3D visualization (FIB – tomography) of eutectic Si in an AlSi7 alloy : (a) flake-like morphology in unmodified condition and (b) fibrous morphology after addition of 170 ppm Sr [18].

It has been reported that an addition of ~280 ppm Sr to an AlSi8.3Cu2Mg0.3FeZnMn0.2 alloy is needed to achieve a full modification from flake-like to fibrous eutectic Si structures (compare Fig. 5 (a-f) vs (g-l)). However, Sr exceeding this value will provoke the formation of non-beneficial phases such as Al_2Si_2Sr [19].

Furthermore, it was observed that rare earth (RE) elements such as La and Ce have a high affinity to react with Sr and degrade Sr modification effects [26]. Up to 1.5 wt.% RE additions to an A356 (AlSi7Mg) alloy result in an increase in the melting point by ~ 1°C per 0.15 wt.% while the temperature for precipitation of the Al-Si eutectic remains constant. Morphological modification effects only appear above 1.5 wt.% RE metal content. However, an increased content of La may lead to the formation of additional intermetallics which could negatively affect the performance of the alloy [26].

2.1.1.2. Primary Si phase

Silicon crystals are harder and more abrasion resistant than any other phase found in typical Al-Si alloys, which is why they are essential for sufficient wear resistance in piston applications (hardness of Si ~ 11.1 GPa up to 200°C [27]). Typically, primary Si crystals have a cubic diamond lattice structure and, ideally, have octahedral morphology [28-30]. Their growth is believed to occur in three stages: (1) nucleation (non-facetted growth with sphere-like external shape), (2) polyhedron transition on the {111} plane or direct transition from a facetted growth unit and (3) further growth and divergence from octahedral shape leading to hollow hopper crystals and dendritic outgrowth (see Fig. 7) [11,30].
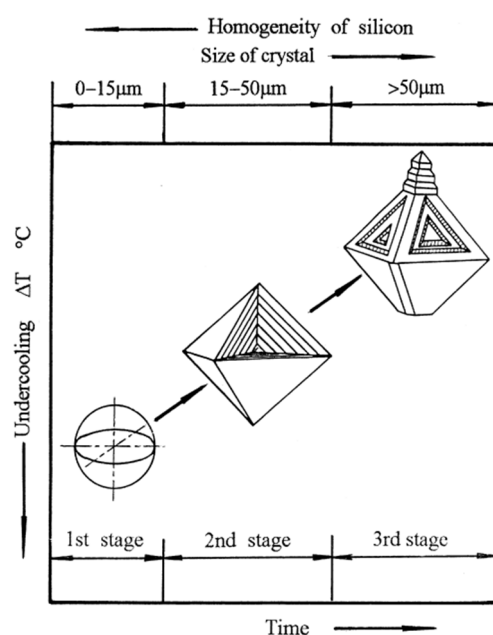
Fig. 7. Three stages of facetted growth of primary Si crystals [28].

Recently, Wang et al. [30] proposed a growth model for primary Si crystals in a cast hypereutectic AlSi20 alloy based on sXCT, SEM, TEM and EBSD observations (see Fig. 8). The most probable primary Si particle morphology was found to have a shape factor of 0.85, which means either regular octahedron or twinned shapes with (edge length (a))/(distance between outer surface and {111} plane (h)) = 2.5 [30].
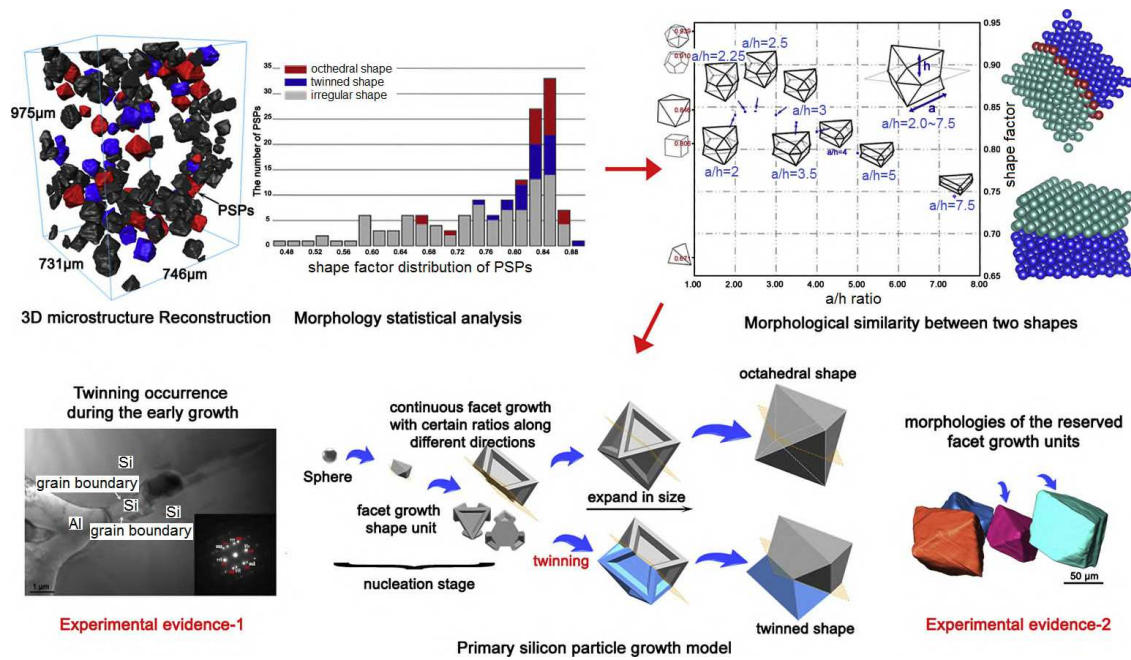
Fig. 8. Growth model for primary Si particles in an AlSi20 alloy based on sXCT, SEM, TEM and EBSD [30].

However, primary Si particle morphologies differing from perfect octahedral and twinned shapes may occur owing to the influence of the surrounding microstructure. For instance, a statistical analysis of 1000 primary Si particles in a high-pressure die-cast hypereutectic A390 (AlSi17Cu4.6Mg0.6) alloy revealed that equivalent diameter and shape factor of those particles are unimodally distributed with peaks corresponding to 25 µm and 0.78, respectively. This significant growth and morphological transition compared to regular octahedral shape (shape factor = 0.85) most likely results from the constraint from Cu-rich phases present in the alloy. The restriction of α-Al grains by the Cu-rich phase exerts stress on the Si particles and thus, causes the occurrence of multiple and/or parallel twinning leading to growth transitions (see Fig. 9) [29].
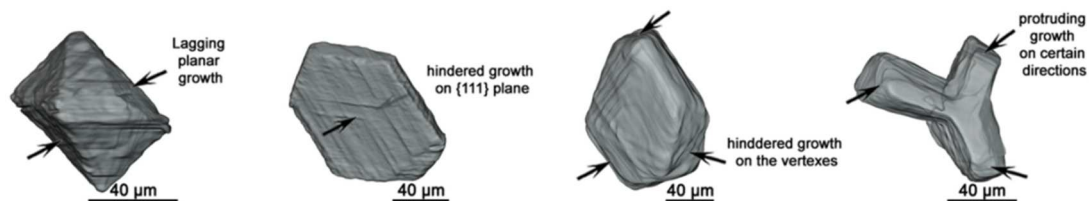
Fig. 9. 3D visualization of primary Si particles with atypical or irregular shapes in a hypereutectic A390 alloy [29].

Primary Si refinement: Effect of Phosphorus

One of the main issues when casting Al-Si alloys is how to control the size and distribution of primary Si particles in order to minimize negative effects on tool life during machining while upholding satisfactory wear performance [11]. A common

approach is to increase the sites for primary Si crystal nucleation complemented by high cooling rates during casting [11,16,18]. This can be achieved by adding P to the melt, which reacts with Al to form small, insoluble AlP_3 particles that can act as nucleation sites for primary Si crystals owing to their very similar crystal structure (diamond cubic) and lattice spacing [11,31,32]. AlP_3 nuclei can usually be observed within refined primary Si particles (see Fig. 10, top right corner) [33,34]. It has been found that P additions between 20 – 40 ppm to the hypereutectic binary melt already contribute to grain refinement. The optimum amount of P in near eutectic Al-Si alloys lies between 40 – 80 ppm. Slow solidification rates and insufficient nuclei provided by P result in the formation of few, very coarse and irregular primary Si crystals (see Fig. 10 (a)). On the other hand, sufficient P content provides an abundance of sites at which primary Si crystals can form and grow and thus, results in a microstructure with many smaller sized, comparatively regular primary Si crystals with more homogenous distribution (see Fig. 10 (b)) [33,34].
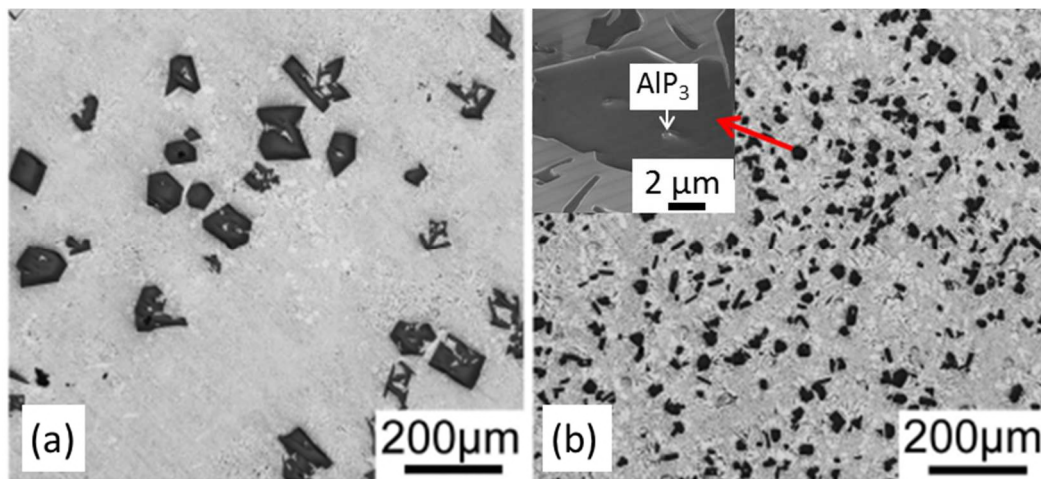
Fig. 10. Effect of P-content on the microstructure of a cast AlSi18 alloy: (a) P = 0 ppm, (b) P = 300 ppm; top left corner: SEM image showing a primary Si crystal containing an AlP_3 nucleus [33].

The refined primary Si particle (AlP_3 nucleated) size depends on solidification rate and other process parameters such as melt flow, melt cooling during flow or thermal patterns during the casting process. However, typical expected primary Si crystal sizes would be 35 – 50 µm for sand castings, 25 – 40 µm for permanent mold castings and 10 – 25 µm for high pressure gravity die castings [11].

For Al-Si (16-23 wt.%) alloys, it has been reported that refinement can be achieved even without artificial nucleation during conventional high pressure die casting. This is most likely owing to exceptional undercooling and rapid solidification rates (typically > 100°C/s), the extremely turbulent flow and also the effect of high

terminal pressures (> 140 MPa) during casting. However, the casting process has to be perfectly controlled to achieve uniformity of the primary Si size, which is rather difficult to achieve and thus, the addition of P is preferred by die casters to ensure consistent results [11].

Elements which can modify both, the eutectic and hypereutectic phase, simultaneously, have yet to be found. Attempts to modify and refine the microstructure using P together with modifier elements like Na, Sr, Ca or Sb revealed that P and those elements react with each other to form compounds which cannot achieve refinement or modification. Only if one of the additives remains in excess can refinement of primary Si *or* modification of eutectic Si be accomplished, but not both [11,34].

2.1.1.3. Intermetallic phases

The composition of near eutectic Al-Si alloys for piston applications is typically characterized by a near eutectic Si concentration (~11-13 wt.%) and the addition of < 10 wt.% of other alloying elements. Usually 1-2 wt.% Ni, 3-5 wt.% Cu and up to 1 wt.% Mg as well as traces of elements such as Fe, Mn, Cr, Ti, V, Zr or P are added
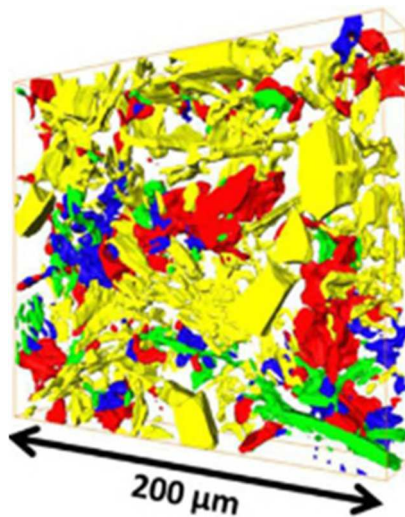

[8,12]. The resulting microstructure shows increased complexity and typically contains an α-Al matrix as the main constituent and interconnected 3D hybrid networks of eutectic and primary Si as well as Ni-, Cu-, Fe- and Mg-containing intermetallic phases (see Fig. 11) (e.g. [14,35-39]).

Fig. 11. 3D visualization of the hybrid network in a cast AlSi12Cu5Ni2MgFe alloy acquired by light optical tomography (voxel size = 0.4 x 0.4 x 1 μm^3): Si (yellow), Ni-rich (blue), Cu-rich (red) and Fe-rich intermetallic phases [39].

The formation of these multicomponent intermetallic phases has been investigated in modifications of the Al-Si-Cu-Ni-Fe-Mg-Mn system (e.g. [40,41]). In this system, considering the range of commercial engine alloys, intermetallic phases such as ε-Al_3Ni (42 wt.% Ni), θ-Al_2Cu (52.5 wt.% Cu), M-Mg_2Si (63.2 wt.% Mg, 36 wt.% Si), δ-Al_3CuNi (~ 30 wt.% Ni, ~ 31 wt.% Cu), γ-Al_7Cu_4Ni (38.7 – 50 wt.% Cu, 11.8 – 22.2 wt.% Ni), T-Al_9FeNi (4.5 – 14 wt.% Fe, 18 -28 wt.% Ni), β-Al_5FeSi (25 – 30 wt.% Fe, 12 – 15 wt.% Si), π- $Al_8Fe_3Si_6$ (10.9 wt.% Fe, 14.1 wt.% Mg, 32.9 wt.% Si),

$Al_{15}(Fe,Mn)_3Si_2$ and Q-$Al_5Si_6Cu_2Mg_8$ (20.3 wt.% Cu, 31.1 wt.% Mg, 27 wt.% Si) may form [9,12,27,38,40,41]. Fig. 12 displays the typical 2D microstructure and identified phases of a cast AlSi12Cu3Ni2MgFe alloy, which is similar to the alloys investigated in this thesis [38].
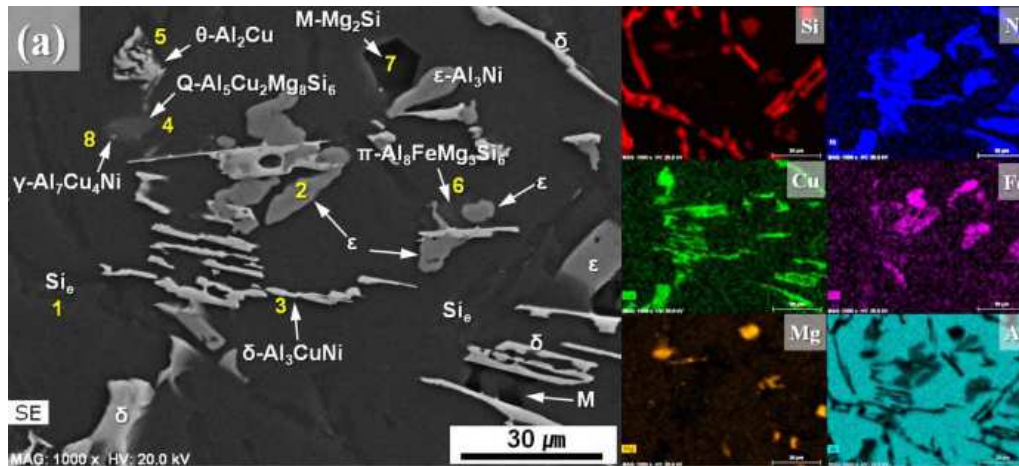
Fig. 12. SEM micrograph (left) and corresponding EDX mappings of an AlSi12Cu3Ni2MgFe alloy revealing different intermetallic phases, eutectic and primary Si embedded in the α-Al-phase [38].

The solidification path of commercial alloys generally does not follow the equilibrium route, thus the alloys are not in thermodynamic equilibrium after casting due to fast solidification rates, which allow for the presence of metastable phases within the cast microstructure [12,40,41].

For an Al-Si-Cu-Ni-Fe-Mg system, Ni:Cu- and Ni:Fe-ratios affect the phase formation during solidification [40,41]. The γ-phase forms for Ni:Cu < 0.25, while the δ-phase will preferentially form for Ni:Cu > 0.25 . Above Ni:Cu > 1.5, ε-phase forms. Above Ni:Fe ~ 2, all Fe within the alloy will most probably be bound to Ni in the T-phase, while the formation of the β-phase will be suppressed [41]. Furthermore, the solidification rate has significant influence on the phase stability and morphology [9,38,42]. Rapid solidification rates generally lead to a decrease in size of all types of intermetallic phases [9,38]. Moreover, they may lead to the absence of ε- and T-phases due to their very narrow solidification ranges [40,41]. γ- and δ-phases may show a transition from coarse structures and clusters towards smaller structures and Chinese script morphologies [9]. An investigation of the elemental concentration of Cu and Ni in an as-cast AlSi10Cu5Ni2 piston alloy revealed a higher concentration of Cu on the surface of a large Cu-, Ni-rich aluminide (see Fig. 13 on top of the specimen), while Cu and Ni are rather homogenously distributed in the inside of the particle, indicating that the alloy in as-cast condition does not seem to have been fully stabilized during solidification [42].
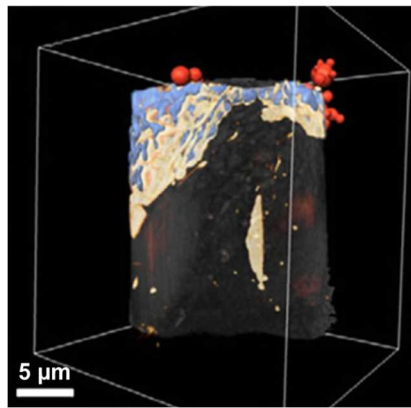
Fig. 13. 3D elemental distribution of Ni (blue), Cu (yellow) and Au (red, used as marker for better alignment of tomographic data and reconstruction) of a Ni-Cu-rich aluminide in an as-cast AlSi10Cu5Ni2 piston alloy acquired by 3D elemental sensitive imaging using transmission X-ray microscopy (voxel size = (24 nm)³) [42].

2.1.2. Effect of solution heat treatment

The effect of solution heat treatment (ST) on the 3D networks formed by Si and intermetallics in cast Al-Si alloys has been studied extensively (e.g. [14,15,18,36,43-48]).

Spheroidization of Si

Thermal treatments of near eutectic Al-Si piston alloys in a range 500°C ≤ T ≤ 560°C typically result in the spheroidization of eutectic Si (e.g. [14,15,43,45,49,50]). This phenomenon occurs in two stages (see Fig. 14): (1) fragmentation at the thinnest parts of acicular eutectic Si particles and (2) rounding and coarsening of the separate parts with progressing ST time (see Fig. 14 (a)) [45,51]. In the case of modified Al-Si alloys, spheroidization occurs at an early stage during ST (see Fig. 14 (b)) [18,51].
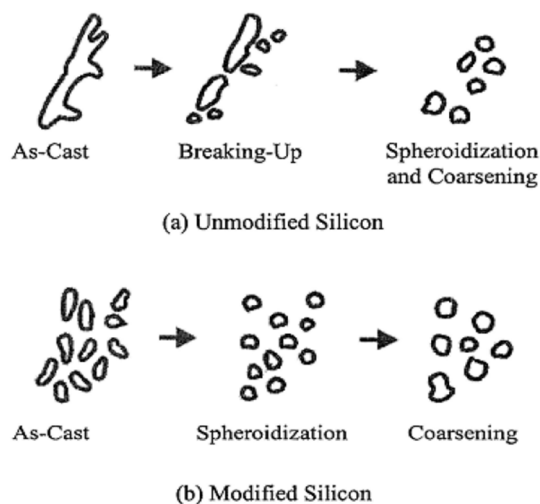
Fig. 14. Schematic illustration of the two stages of spheroidization of eutectic Si for (a) unmodified and (b) modified cast Al-Si alloys [51].

The morphological change of Si particles during solution treatment is caused by the surface tension that tends to minimize total-free-energy or the interface area/particle-volume ratio (S/V). Fig. 15 shows the effect of ST at 540°C for 4 hours on morphology and global interconnectivity in an unmodified AlSi12 alloy. The spheroidization of Si results in the disintegration of the 3D network of eutectic Si lamellae and thus, leads to a loss of global interconnectivity [47].
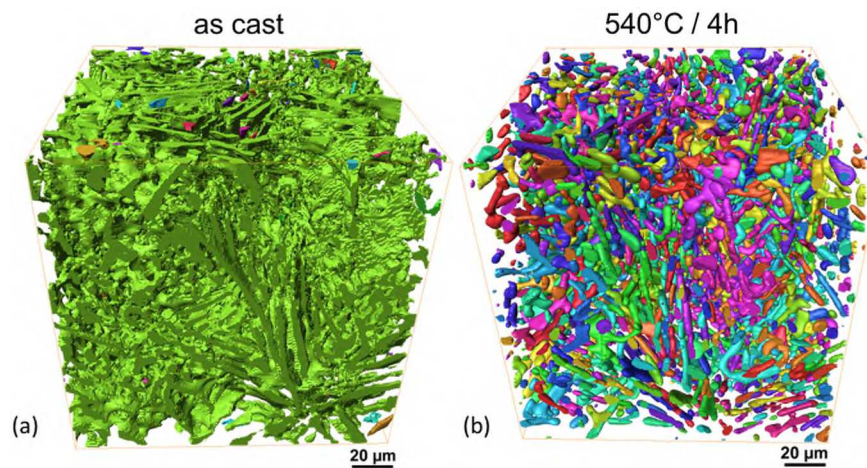
Fig. 15. 3D network formed by eutectic Si in an unmodified AlSi12 alloy in (a) as cast condition and (b) after ST at 540°C for 4 hours. Images acquired by synchrotron holo-tomography [47].

The determining factor of the time needed for complete spheroidization is the thickness and morphology of Si platelets [45]. For cast unmodified and Na-modified AlSi(9 - 13 wt.%) alloys, it was found that spheroidization of eutectic Si during solution treatment at 550°C occurs within the first 15 min of heat treatment [50].

Effect on intermetallic phases

Besides Si spheroidization, ST can also result in the (partial) dissolution of intermetallic phases such as Mg_2Si and Al_2Cu (e.g. [43,49]). Especially Ni- and Fe-rich aluminides are, from a topological point of view, fairly stable below the eutectic point and only slight global changes in volume fraction, interconnectivity and morphology can be detected for alloys with near eutectic composition and additions of Cu and Ni (see Fig. 16 (a-b)) [14,48,52]. Generally, Si spheroidization is more pronounced in the case of binary near eutectic Al-Si alloys and it decreases as the volume fraction of aluminides increases [49,52]. It has been shown that the addition of 1-2 wt.% Ni to a binary AlSi12 alloy can form a long-range 3D hybrid network and has a retarding effect on the disintegration of the Si network during ST. Contrarily to AlSi12, the networks in the AlSi12Ni alloy remain highly interconnected after ST (540°C/24h) owing to high contiguity between aluminides and Si (see Fig. 16 (c-f)), grey areas indicate contiguity between Si and aluminides) [14,47,52,53].
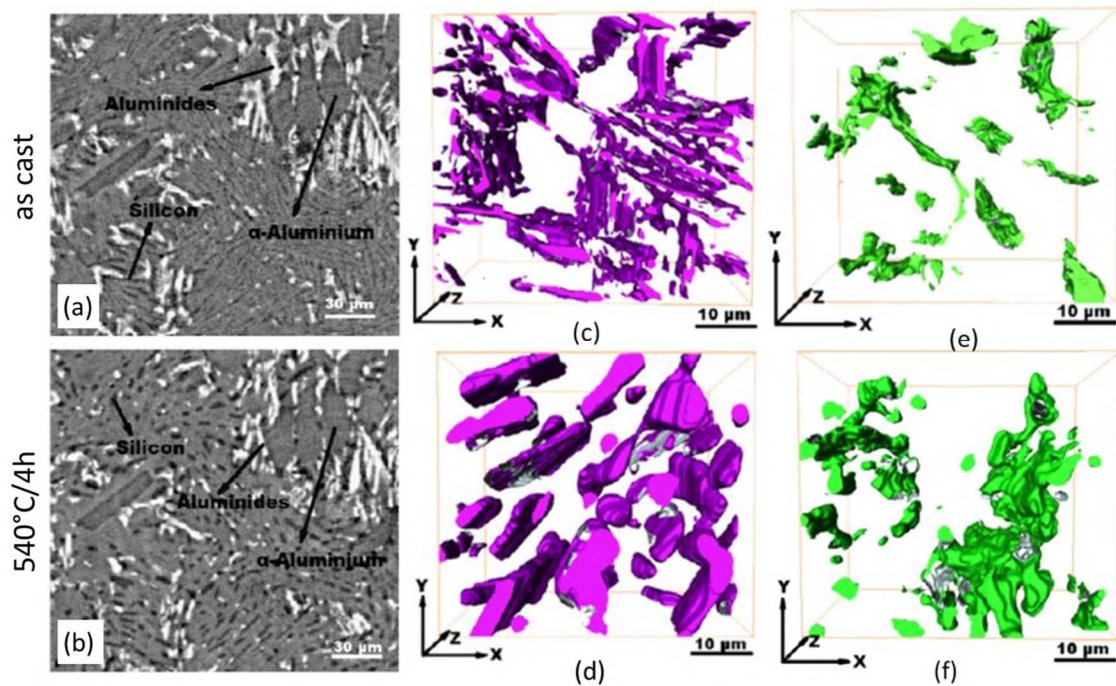
Fig. 16. AlSi12Ni alloy before (a,c,e) and after ST at 540°C for 4 hours (b,d,f): (a-b) synchrotron tomography slices (voxel size = (0.3 μm)³), (c-d) 3D visualization of Si and (e-f) 3D visualization of aluminides. [52]

2.2. Strength of cast Al-Si alloys

The mechanical properties of Al-Si piston alloys depend on their casting structure and on microstructural features such as grain size, secondary dendrite arm spacing (SDAS), size, precipitation condition and architecture of eutectic and primary Si as well as of intermetallic phases and casting defects [44,46]. Features providing strength in cast Al-Si piston alloys can be summarized as follows: precipitation hardening, solid solution strengthening, grain size and dendrite arm spacing, strain hardened regions and the load partition between Al-matrix and rigid phases.

2.2.1. Casting defects

The most common casting defects in Al-Si alloys are porosity and inclusions whose formation/presence and distribution strongly depends on the condition of the melt, the manufacturing process and thermal treatments. Depending on their size and morphology distribution, casting defects can significantly degrade the alloy's performance. High Cu and Mg contents promote the formation of shrinkage porosity (e.g. for A356 (AlSi7Mg) this is particularly relevant for Cu contents > 0.2 wt.% [54]). An increase of porosity level and pore size has adverse effects on mechanical

properties of cast Al-Si alloys (e.g. [17,55-58]). Pores cannot bear mechanical loads and are usually stress concentration sites, resulting in the formation and propagation of microcracks [54]. Investigations of unmodified AlSiXCu4Ni3Mg alloys with 0.67 wt.% ≤ X ≤ 12.5 wt.% (< 0.1 vol.% of casting porosity for all alloys) under fatigue conditions revealed that in the case of the AlSi(0.67 wt.%) alloy, crack initiation was predominantly associated with large clusters of casting porosity (max. pore diameter > 400 μm). However, casting pores with max. pore diameter ~ 210 -240 μm play a minor role as crack initiator for Si contents > 6-7 wt.%. In this case, crack initiation was observed to occur predominantly at Si and (Cu, Ni, Fe)-rich intermetallic phases [57,58].

2.2.2. Precipitation strengthening

Cu and Mg contribute to the strengthening of Al-Si alloys in a temperature range 25°C ≤ T ≤ ~200°C owing to the formation of precipitates such as θ-Al_2Cu, M-Mg_2Si and/or S-Al_2CuMg (see Fig. 17) [59]. However, at temperatures above 200°C, the strengthening effect is lost owing to dissolution or Ostwald ripening [59,60].
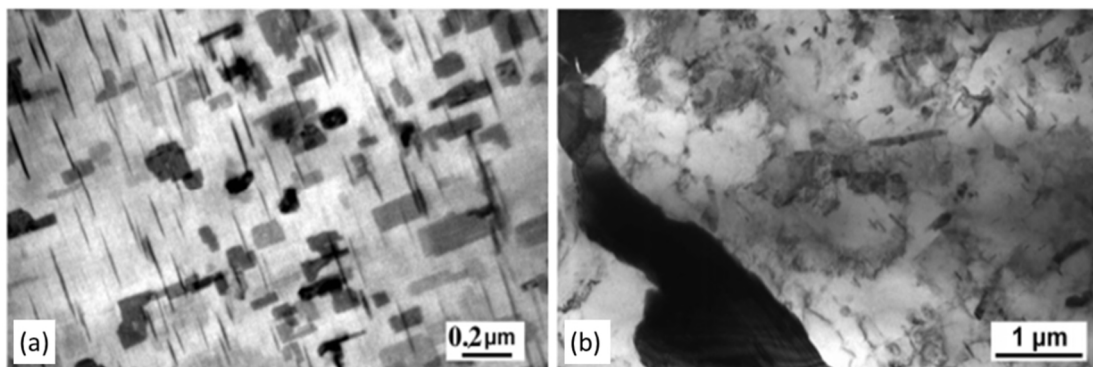
Fig. 17.TEM micrograph of Al_2Cu/Mg_2Si/Al_2CuMg platelets in a cast AlSi12CuNiMg alloy: (a) after aging (T6), (b) after exposure at 300°C during tensile testing [59].

The addition of traces of alloying elements such as Zr and Ti, which are hardly dissolvable in the α-Al-matrix, results in enhanced high temperature stability of the alloy (solid solubility of Zr in Al = 0.28 at.% at 660.5°C - peritectic reaction L + Al_3Zr ↔ (Al) and 0.05-0.06 at.% Zr at 427°C; solid solubility of Ti in Al = 1.3 at.% at 665°C - peritectic reaction L + Al_3Ti ↔ (Al) and 0.2-0.3 at.% Ti at 527°C [12]) [22,61]. Ti acts as a substitute for Zr in metastable $Al_3(Zr,Ti)$ $L1_2$ structured precipitates which are found to nucleate homogeneously in high number densities during the decomposition of supersaturated solid solution in the center of dendrites. They are more resistant to coarsening and thermodynamically more stable than the

traditional secondary Mg_2Si and Al_2Cu precipitates, thus, these coherent particles provide strengthening even above 200°C. Depending on processing conditions, they occur in various morphologies such as rod-like, petal-like, cauliflower, cellular or disk-like shapes [62-64]. Fig. 18 shows $L1_2$ spherical Al_3Zr nano-particles in Al-0.22wt.%Zr (Fig. 18 (a)) and cauliflower-shaped ones in Al–0.1 Zr–0.1 Ti(b) alloys (Fig. 18 (b)) after ageing at 425°C for 100h and 400h, respectively [62,63]. Fig. 18 (c) shows disk-shaped thermodynamically stable tetragonal $D0_{23}$ precipitates with 150–200 nm in diameter and 50–60 nm in thickness and three possible orientations [64]. Al_3Zr ($L1_2$) particles were found to remain coherent up to 400h at 375°C or 425°C at the center of dendrites, while a loss of coherency was detected at the periphery of dendrite branches after aging at 375°C/400h [63]. The transition from coherency to semi-coherency was found to occur at a radius of about 35 nm for Al_3Zr ($L1_2$) precipitates [62]. Furthermore, this was also the radius at which surface perturbations responsible for the cauliflower shape in Fig. 18 (b) could be first observed [63].
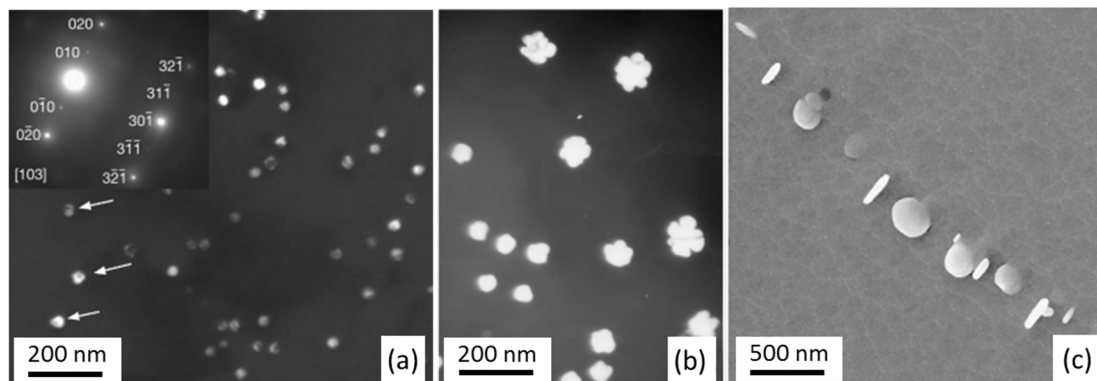
Fig. 18. TEM dark field image of (a) fine spherical $Al_3Zr(L1_2)$ precipitates in an Al-0.22wt.%Zr alloy aged at 425°C/100h, (b) Cauliflower shaped $Al_3(Zr_{1-x},Ti_x)$ ($L1_2$) precipitates in an Al–0.1 Zr–0.1 Ti(b) alloy aged at 425°C/400h and (c) disk-like Al3Zr ($D0_{23}$) precipitates in Al–0.1Zr(b) aged at 500°C for 100 h (after peak aging at 375°C for 100 h) [62-64].

The loss of coherency was also proposed to contribute to the growth instabilities in interdendritic $L1_2$ particles [62]. After ageing at 460°C in a time range of 24h $\leq$ t $\leq$ 700h, a size increase of $L1_2$ Al_3Zr particles from 20 to 70 nm was reported in [65].

Amounts of Zr > 0.2 wt.% promote the formation of large, brittle needle-like particles attached to primary phases which have detrimental effect on the mechanical performance [62].

Modification of Al_3Zr ($L1_2$) particles can be achieved by additions of Yb, which promotes a two-peak hardening during isochronal ageing due to $Al_3(Zr,Yb)$ precipitation owing to higher coarsening- and creep-resistance compared to Al_3Zr or Al_3Yb [66]. Also, an addition of Zr, Sc and Er results in the formation of coherent,

spheroidal, L1$_2$-ordered Al$_3$(Zr,Sc,Er) precipitates consisting of an Er-enriched core surrounded by a Sc-enriched inner shell and Zr-enriched outer shell. These particles were found to provide excellent coarsening and creep resistance at 400°C [67].

2.2.3. Solid solution strengthening

Mg and Cu contribute to increasing creep resistance and retarding the strength degradation at elevated temperatures by strengthening the α-Al-matrix [59,68]. Even though the effect of solid solution strengtheneing is negligable at room temperature (RT) (only 0.05 wt.% of Cu is soluble in Al), at temperatures up to 200°C, hardness, ultimate tensile strength (UTS) and yield strength (YS) are increased owing to the higher solubility in Al [12,69]. Nevertheless, solid solution strengthening provided by the alloying elements Mg and Cu is limited. Mg contents > ~ 0.7 wt.% [69] do not result in further strengthening but decrease the plasticity of heat treated Al-Si alloys owing to the formation of intermetallic phases such as Mg$_2$Si, Al7Cu4Ni, Al4Cu2Mg8Si7 and AlSiFeNiCu [45,68,70,71]. Other major alloying elements such as Si (max. solubility in Al = 1.6 wt.%), Ni and Fe (solubility in Al = ~ 0.04 wt.% at eutectic temperatures 640°C and 655°C, respectively) do not provide any significant solid solution strengthening effect [12,72].

2.2.4. Strain-hardened regions

Intermetallic phases in Al-Si alloys display a thermal expansion coefficient (CTE) between 12 - 17 ppm/°C, while Si has a CTE of 3.4 ppm/°C. Both are smaller than that of the α-Al matrix (26.3 ppm/°C) [27,62]. The different CTE between rigid phases and α-Al, can promote strain-hardened regions during solidification or cooling from heat treatment temperature. This is especially relevant for Si/Al-matrix interfaces, since Si shows the largest difference in CTE compared to the soft α-Al-matrix. This type of strengthening is typical for metal matrix composites and shows its effect especially at RT. However, at elevated temperatures, the strengthening effect is lost owing to relaxation processes [73].

2.2.5. Grain size and dendrite arm spacing

Coarse microstructures, i.e. large secondary dendrite arm spacing (SDAS), in general, show higher sensitivity towards damage initiation, enhancing the probability of failure [74]. Small SDAS commonly helps to improve the thermo-mechanical properties of cast Al-Si alloys [9,19,74,75]. For a cast AlSi8Cu2Mg0.3FeZnMn0.2 alloy an increase of SDAS from 10 to 50 µm (achieved by varying solidification rates) was found to result in a decrease of tensile strength by ~ 50% and elongation at fracture by ~ 80% [19]. Fig. 19 illustrates the superior tensile strength of a fine microstructure (SDAS = 10 µm) compared to a coarser one (SDAS = 25 µm) in a temperature range $RT \leq T \leq 500°C$ for the aforementioned alloy [19].
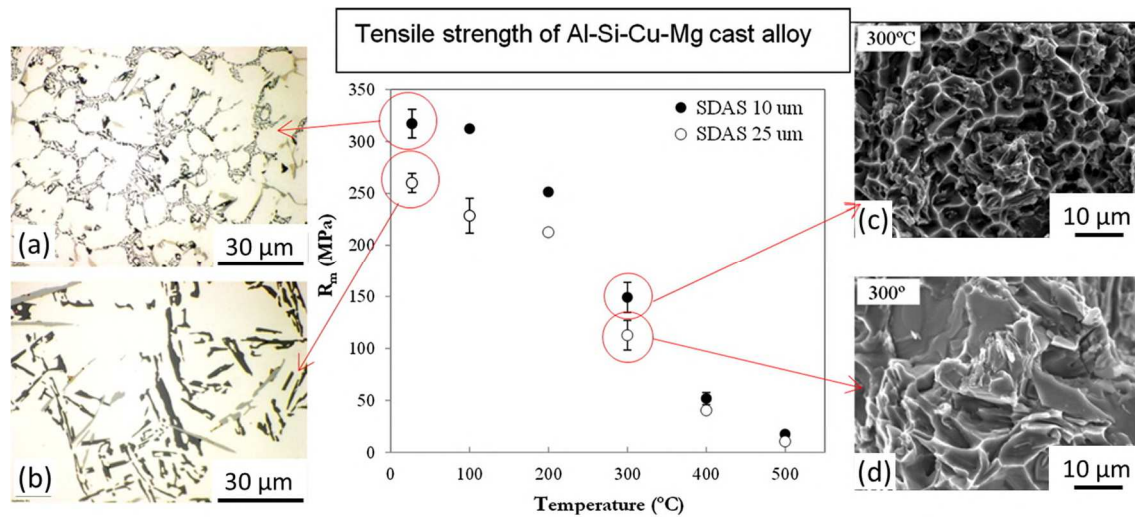
Fig. 19. Ambient and elevated temperature tensile strength of a cast AlSi8Cu2Mg0.3FeZnMn0.2 alloy in dependence of SDAS [19].

A decrease in SDAS (from 84.1 µm to 0.82 µm) and grain size provoked by increasing the solidification rate (from 0.15 to 1.5×10^5 °C/s) of an AlSi13Cu4Mg2Ni alloy was found to result in an increase of Brinell hardness by about 64% and RT tensile strength by about 49% [9]. Very fine grain sizes and structures (SDAS ~ 0.8 - 2 µm) acquired by controlled laser-melting promote excellent thermo-shock and fatigue-resistance of near-eutectic Al-Si alloys [7,75]. It was observed that the local re-melting of the bowl rim area of automotive pistons results in an increase of fatigue properties by 90% compared to the cast piston in this critical area. This method provides higher process stability compared to the casting process, however, production costs are very high [7].

2.2.6. Morphology and size distribution of rigid phases

<u>Eutectic and primary Si</u>

The amount of Si in Al-Si alloys has been found to have significant effects on mechanical properties such as Young's Modulus, YS, UTS as well as corrosion and wear resistance of Al-Si alloys [55,76,77]. An increase of Si content typically results in a decrease of thermal conductivity and ductility [78]. The RT mechanical properties of cast binary Al-Si alloys with Si contents in a range from $2 \leq$ Si wt.% $\leq$ 20 were tested in [78]. It was reported that Vicker's hardness shows a continuous increase with increasing Si-content, while UTS and YS reach a maximum (189 MPa) at 12.5 wt.% Si followed by a decline with further increasing Si-content. Elongation at fracture displays a continuous decrease with increasing Si-content (see Fig. 20) [78]. Furthermore, at 250°C, the increase of Si-content from 7 to 12 wt.% in a cast Al-Si alloy was observed to improve UTS by ~25 MPa and YS by ~ 20 MPa [72].
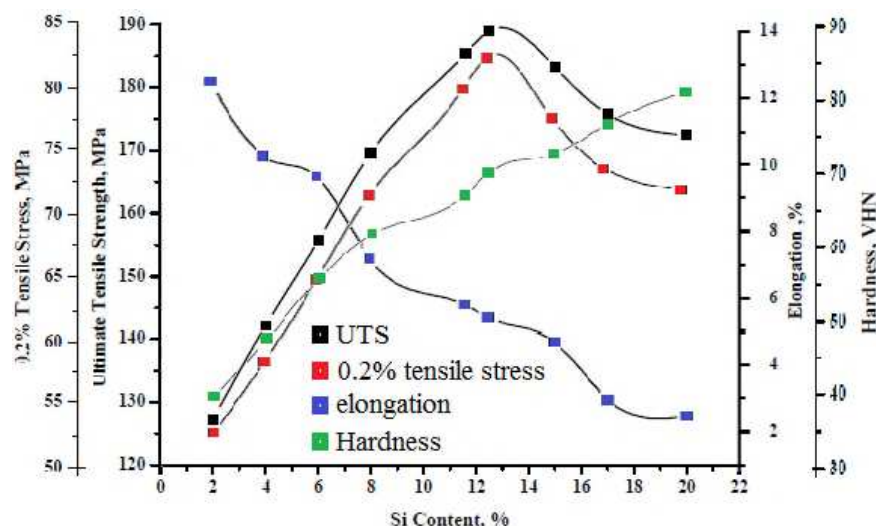
Fig. 20. Effect of Si content on UTS, YS, elongation and Vickers-hardness of an Al-Si alloy [78].

Eutectic and primary Si are known to play a decisive role in damage formation and accumulation of cast Al-Si alloys. It has been suggested that microstructural extrema like the largest Si particle size are the controlling factors of fracture and ductility of Al-Si alloys rather than the average microstructural features [79]. For better mechanical performance, fine, fibrous eutectic Si morphologies are preferable to flake-like ones (see Fig. 6 (a) vs (b)) [18,20]. Those structures result in a change of fracture mode from transgranular/brittle to intergranular and thus, enable higher ductility and UTS [19,80,81]. Microscopic three-point bending tests to measure the strength of coarsened eutectic Si particles extracted from a cast AlSi12.6 alloy

revealed that microstructural flaws, such as pinholes and particularly trench-like interfaces along their facets, can drastically reduce the strength (typically 9 GPa) of these particles and thus, limit their reinforcing capability [82]. Joyce et al. reported that the primary Si morphology is the controlling factor for fatigue crack growth in near eutectic Al-Si alloys [83]. Generally, fracture of Si particles in Al-Si alloys was reported to appear in three stages: (1) cracks initiate at Si particles, (2) propagation of cracks throughout interdendritic regions and (3) fracture of the Al matrix [84]. Fracture in eutectic A413.1 (AlSi11.7Cu(0.8-2.8)Ni(0.02-1.4)Mg(0.08-0.4)) automotive alloys during RT tensile deformation was reported to preferentially occur at brittle acicular Si particles rather than spherical ones [44]. Several works indicate that the fraction of fractured Si particles in alloys with small and uniform primary Si is always less than that in alloys with large, non-uniform Si particles owing to a size effect [57,85,86] and to possible flaws such as sharp edges or narrow junctions between coalesced particles (see Fig. 9) (e.g. [44,46,57,74,84, 86]).

Intermetallics

Cast Al-Si microstructures which contain intermetallic phases have frequently been reported to exhibit increased tensile strength at ambient (e.g. [87-90]) as well as elevated temperatures (e.g. [14,36,91-94]) compared to binary alloys. On the other hand, the interaction between alloying elements such as Si, Cu and Mg can have a negative effect on the elevated temperature tensile strength owing to the formation of brittle intermetallics (e.g. $Al_5Mg_8Cu_2Si_6$) which can serve as crack initiators during tensile deformation [95]. Moreover, besides porosity and oxides, Fe is one of the most common impurities and prone to be present in brittle intermetallic phases with undesired needle-like morphologies (primarily Al_5FeSi, β-phase) which reduce ductility and fatigue resistance [96,97]. Especially in coarse microstructures (SDAS > 20 μm) large Fe-rich intermetallics were observed to play a predominant role in damage formation and propagation (cracks with lengths up to a few hundred μm) [19,98].

Furthermore, volume fractions of connected rigid phases > ∼ 5 vol.% may result in damage onset at early stages during deformation [36,49,52]. Closely packed rigid particles can facilitate the propagation of damage, leading to abrupt failure of the alloy [99]. For instance, it has been found that damage during tensile deformation in a cast AlSi12Ni alloy is strongly related to the architecture of networks formed by

intermetallic phases [100]. Small clustered aluminide structures are prone to break off at earlier deformation steps than larger ones (see Fig. 21) owing to higher stress concentrations [100].
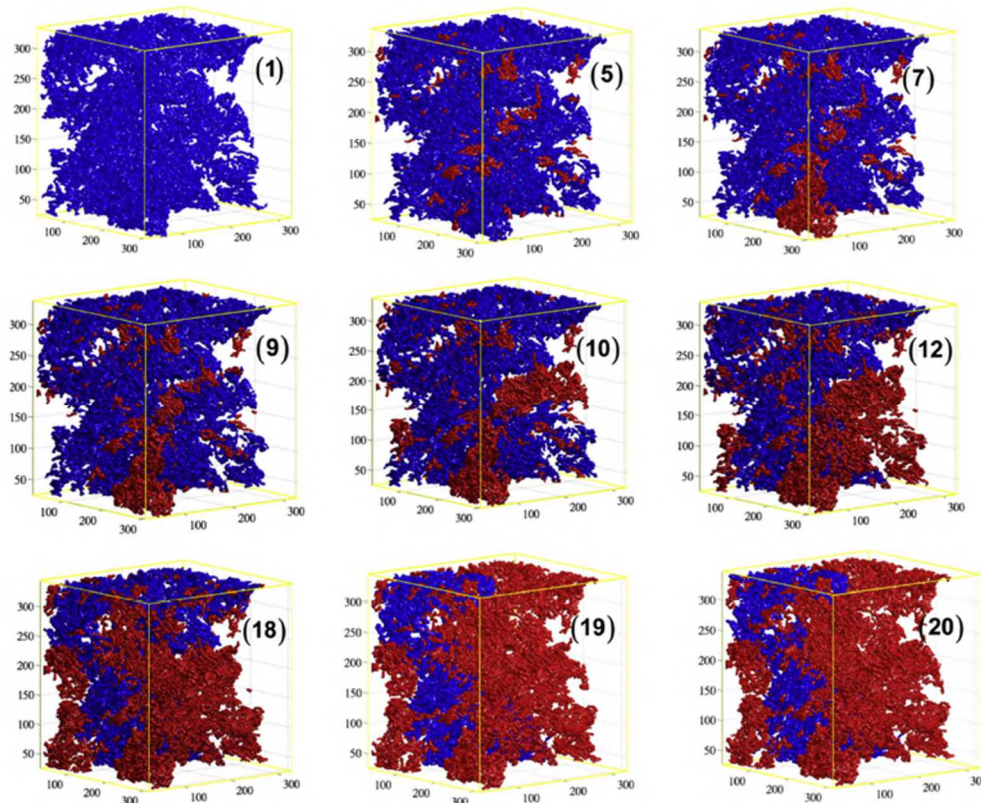
Fig. 21. Damage evolution of a complex intermetallic 3D network from the initial condition until failure in an AlSi12Ni alloy. The parents and sons are colored in blue and red, respectively. Axis-units are given in voxels (voxel size = (1.4 μm)³) [100].

2.2.7. Degree of connectivity

2.2.7.1. Global interconnectivity of the 3D hybrid network

The global interconnectivity, I, of the 3D hybrid networks formed by Si and intermetallic phases plays a relevant role in the mechanical performance of Al-Si alloys at RT and elevated temperatures (e.g. [6,14,15,101]). It is defined for a given volume of material as the ratio between the volume, V, of the largest particle and the volume of all particles of the same phase [14,35,37]:

$$I = \frac{V_{largest\ particle}}{V_{all\ paticles}}, [\%] \text{(Equ. 1)}$$

Fig. 22 shows the strength in several cast Al-Si alloys as a function of solution treatment time. The presence of about 20 vol.% of highly globally interconnected 3D networks formed by eutectic Si and Ni- , Cu-, and/or Fe-rich aluminides leads to

higher strength after solution treatment at 490° compared to the binary AlSi12, which completely loses the global interconnectivity of eutectic Si (see Fig. 22, right side) [12,14,36,48,52,102].
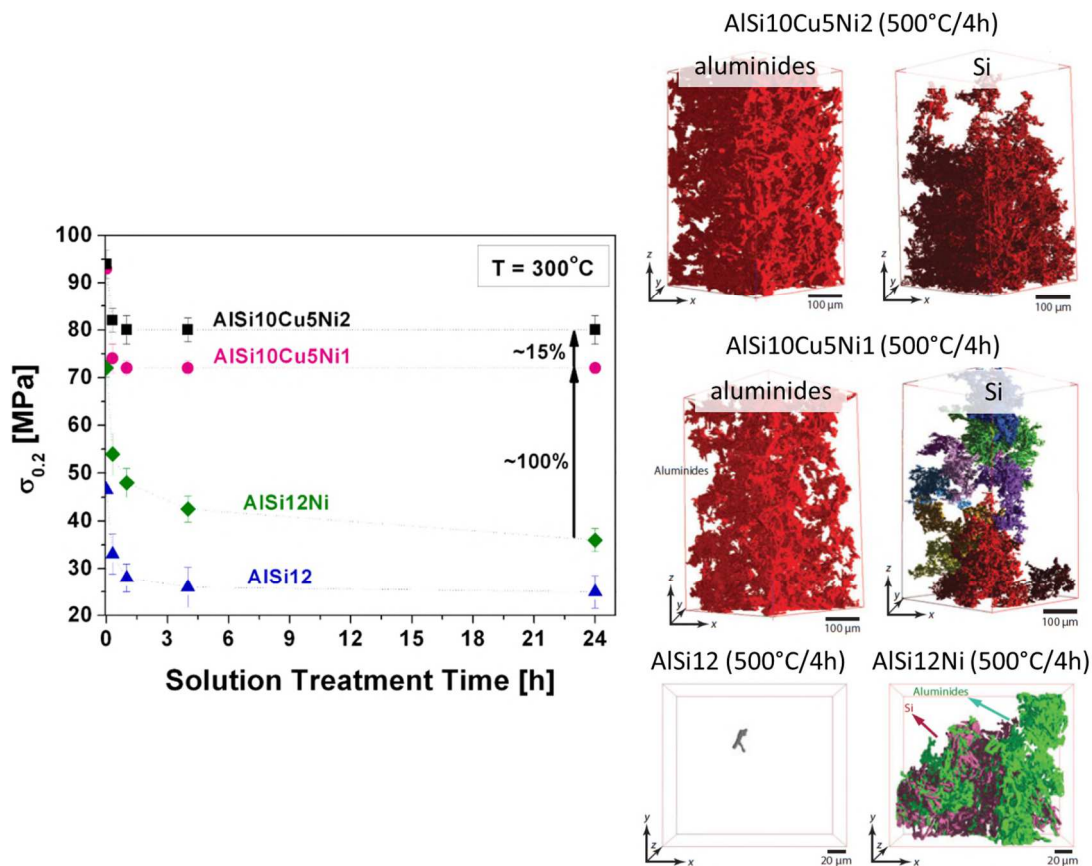
Fig. 22. Proof stress $\sigma_{0.2}$ at 300°C for different Al-Si alloys as a function of ST time at 490°C and corresponding 3D networks of aluminides and Si after ST (490°C/4h) [14,36].

2.2.7.2. Local connectivity – Euler number

Owing to the morphological complexity of the 3D hybrid networks in cast Al-Si alloys, it is insufficient to simply consider the global interconnectivity for a full understanding of their thermo-mechanical behavior. Changes in local connectivity of the 3D hybrid networks (i.e. loss or formation of connecting branches within a 3D network) can take place as a result of thermal treatment or during service while global interconnectivity practically remains constant. These changes can be quantified using the topological parameter Euler number, χ, [103,104,105] which can be calculated as follows:

$$\chi = N + \sum_{i=1}^{N} N_C^i - \sum_{i=1}^{N} N_T^i \quad \text{(Equ. 2)}$$

N ... number of isolated particles
N_C^i ... number of cavities for ith isolated particle
N_T^i ... number of tunnels for ith isolated particle

It has been proposed that a decrease of local connectivity (increase of Euler number) owing to a loss of connecting branches within the 3D network is directly related to a loss of load carrying capability of globally fully connected 3D networks [106,107]. Silva et al. [106] investigated theoretically the strength of a periodic 2D microstructure after randomly removing connections. A loss of 10 % of existing connections within the model material resulted in a decrease of strength by ~35 %. Kruglova et al. [107] correlated also theoretically, an increase in strength of an AlSi7 alloy to a more negative Euler number of the 3D network of eutectic Si (see Fig. 23). The compressive strength of the material was investigated by generating and analyzing virtual 3D microstructures with varying degrees of interconnectivity and branching of Si particles. In their stochastic model, higher branching and lower distances between branches leads to increased local connectivity (see Fig. 23). Furthermore, the strength of the material increases with branching and local connectivity of eutectic Si. This theoretical study has shown that the Euler number can be an effective parameter to characterize local connectivity of 3D networks in Al-Si alloys.
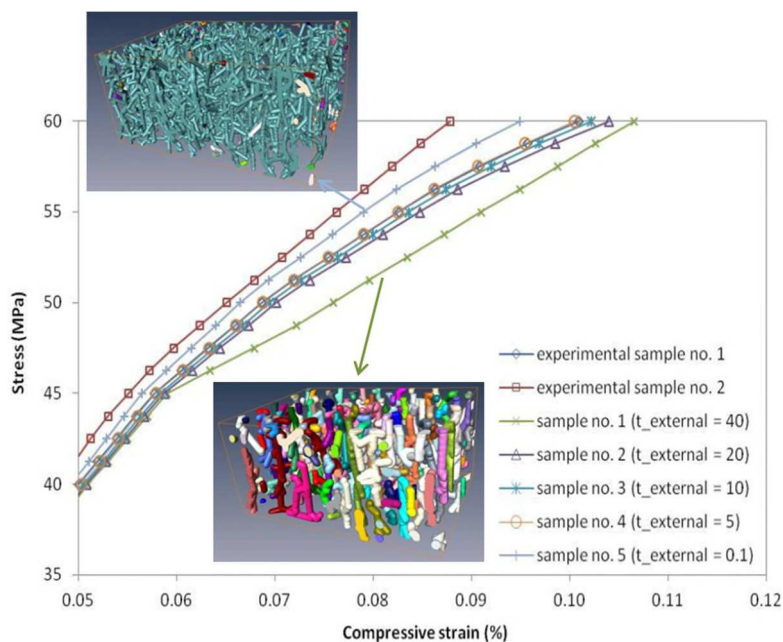
Fig. 23. FEM simulations on virtual structures with different local connectivities of eutectic Si networks in an AlSi7 alloy [107].

2.3. 3D imaging

In the case of Al-Si alloys, 3D characterization methods have proven to be more efficient compared to conventional 2D investigations to reveal non-uniformly

distributed microstructural features that influence damage processes [108,109,110,111]. Tomography provides a non-destructive way to visualize the internal structure of complex materials three-dimensionally in a wide range of spatial resolutions from sub-µm (nano)-range to cm scale (see Fig. 24) [112,113].
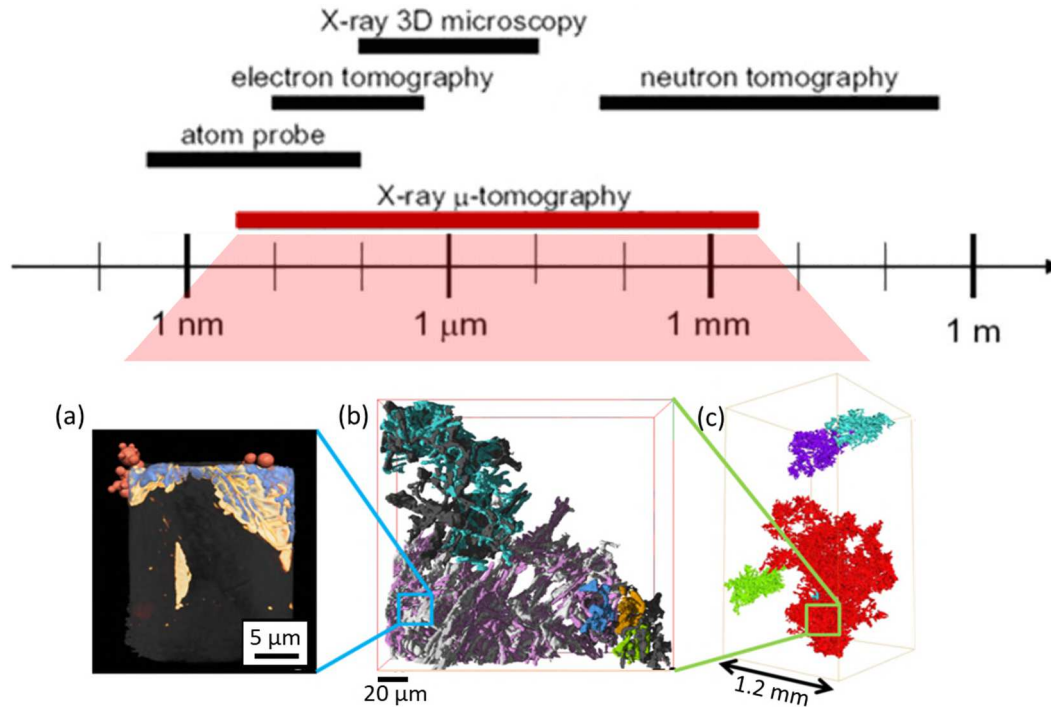
Fig. 24. top: 3D imaging methods and sample sizes (end of the bars) over a range of resolutions (beginning of the bars) from 1 nm to 1 m [113].
bottom: Multiscale X-ray tomography of cast Al-Si piston alloys: (a) 3D distribution of Ni (blue) and Cu (yellow) revealed using K-edge subtraction with a focused synchrotron beam – voxel size = (24 nm)³, (b) larger region studied by parallel beam synchrotron tomography revealing large 3D structures formed by several interconnecting particles of different aluminide types (shown in different colors) – voxel size = (0.3 µm)³, (c) large 3D structures of aluminides revealed by laboratory cone-beam X-ray tomography – voxel size = (3 µm)³. Adapted from [39,42].

2.3.1. X-ray computed tomography

Fig. 24 shows examples of the internal architecture of cast Al-Si piston alloys acquired by multiscale x-ray tomography with voxel sizes between (24 nm)³ and (3 µm)³ [39,42].

Laboratory cone beam x-ray computed tomography (XCT) represents the most common method for non-destructive investigations and 3D characterizations of materials and components [114,115]. Fig. 25 depicts a schematic illustration of a laboratory XCT setup. A cone beam is produced by the X-ray source. Different magnifications can be achieved depending on the sample-to-detector distance. The X-ray beam penetrates the rotating sample and strikes the planar CCD detector. Owing to interactions (photoelectric effect, Compton scattering) within the sample the beam

is attenuated depending on the density, the atomic number of material constituents and the energy of the X-ray beam. Radiographic projections are acquired at several angular positions.
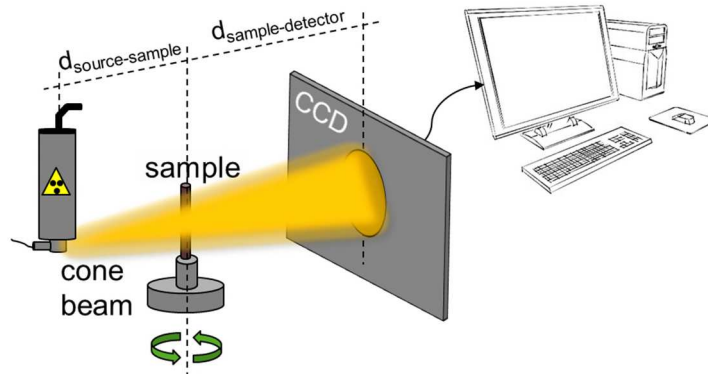
Fig. 25. Schematic illustration of setup for XCT with cone beam geometry.

A number of limitations experienced with laboratory-based XCT can be overcome using synchrotron x-ray computed tomography (sXCT). First of all, the brilliance of 3rd generation synchrotron sources is many orders of magnitude higher than that of laboratory x-ray tubes. This yields images with a high signal-to-noise ratio on short time-scales and thus, enables fast acquisition times. Moreover, the coherence of the beam can be used for quantitative phase contrast imaging [116], while focusing optics can lead to resolutions down to about 50 nm [117,118]. Reviews of the historical development of sXCT can be found in [119,120]. Fig. 26 shows an overview of available energy ranges, achievable minimum voxel sizes and scanning times at synchrotron beamlines with tomographic setups suitable for 3D imaging of metallic structures [120].
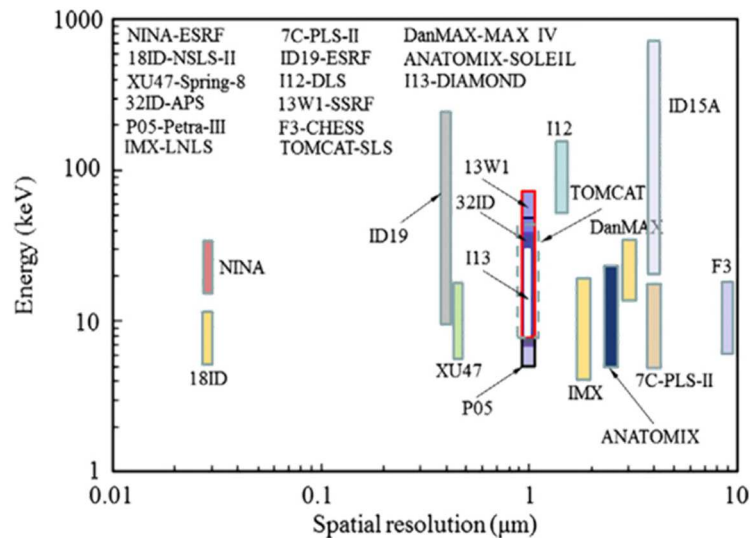
Fig. 26. Overview of capabilities of synchrotron beamlines with tomographic setups [120].

Another advantage of synchrotron sources is the possibility to combine different techniques available at the same beamline, such as simultaneous tomography and diffraction experiments [121].

2.3.2. Contrast imaging mechanisms

Absorption contrast is caused by the difference in the linear absorption coefficients of the material's constituents, i.e. it depends on the atomic number of the elements present, the density of a material and the energy of the X-ray beam [122]. For Al-Si cast alloys, absorption contrast can reveal highly X-ray absorbing intermetallic phases such as Al_7Cu_4Ni, Al_3Ni or Al_9FeNi. However, it is not sufficient to reveal Al and Si separately owing to their very similar X-ray absorption coefficients [14,120], i.e. phase contrast is necessary. For a quantitative utilization of phase contrast, the phase shift of x-rays must be retrieved using techniques such as single-distance phase retrieval [123,124] or the propagation technique holo-tomography [118,125].

Propagation-based imaging relies on the interference of coherent x-rays at interfaces for the enhancement of visibility of edges and boundaries within the material. In holo-tomography, phase retrieval is achieved after scanning the region of interest at multiple sample-to-detector distances (see Fig. 27). Closest to the detector (see Fig. 27, d_1 = 3mm) mainly absorption contrast is achieved. The phase contrast increases with increasing sample-to-detector distance (see Fig. 27) [126,127]. This imaging technique has already been successfully applied for Al-Si alloys [47].
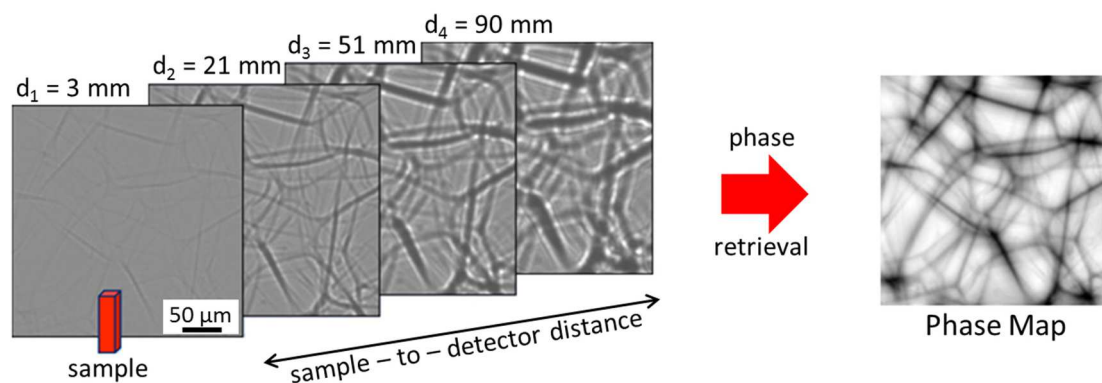
Fig. 27. Phase contrast in radiographies of polystyrene foam achieved by increasing distance between sample and detector [128].

2.3.3. Investigation methods during tomography

The simplest experimental procedures to study the microstructure evolution and damage behaviour of metallic materials are ex-situ investigations of post mortem specimens (different samples at different conditions) or of same specimens after having been subjected to external loads (e.g. conditions with increasing heat treatment time). For damage analysis, more appropriate techniques would be in-situ

investigations where the same sample is investigated under (thermo-) mechanical loading conditions [125]. XCT, with resolutions close to 1 μm but relatively long acquisition times of typically 30 – 200 min is an appropriate tool for interrupted in-situ investigations [111,118,120,129]. Owing to the fast acquisition times (down to less than 1 sec with voxel sizes of ~ $(1 \ \mu m)^3$) [118,129], sXCT is an excellent choice for conducting in-situ investigations [130], e.g. experiments to monitor fatigue crack growth [131,132] or damage evolution during (thermo-) mechanical loading [15,133-137]. Fig. 28 and Fig. 29 (a-b) present a schematic illustration and experimental setups for in-situ synchrotron imaging experiments during tensile testing at ambient and elevated temperatures used in this work [138,139].
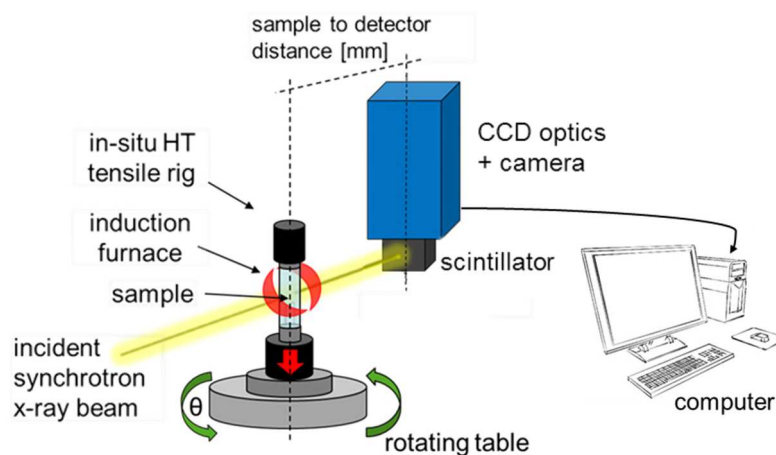
Fig. 28. Schematic illustration of the setup used in this work for in-situ tensile tests at synchrotron facilities.
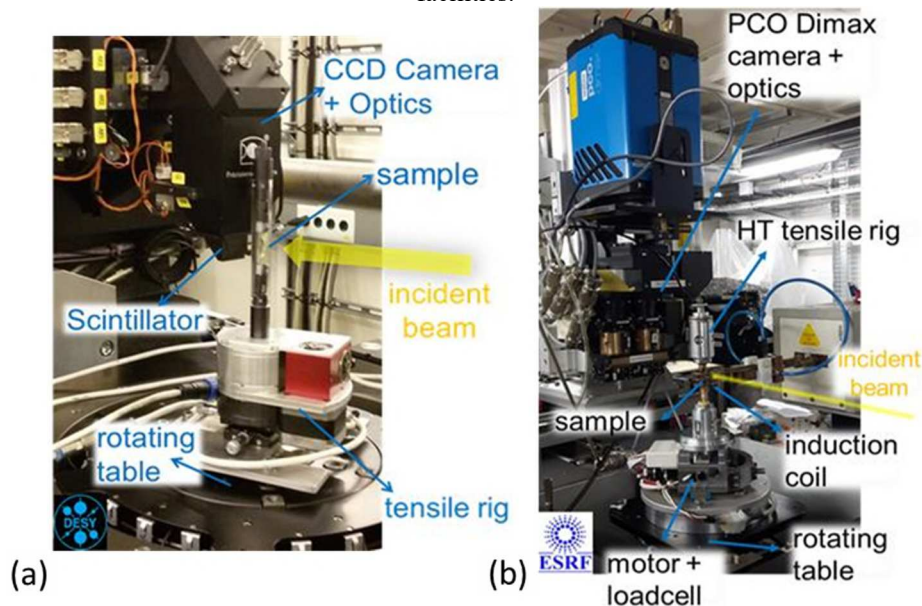
Fig. 29.(a) setup for the interrupted in-situ RT tensile tests conducted at DESY/P05 (tensile rig provided by IMDEA Materials), (b) setup for interrupted in-situ elevated temperature tensile tests conducted at ESRF/ID19 (tensile rig provided by INSA de Lyon)

Chapter 3

SUMMARY OF RESULTS & DISCUSSION

3.1. Hypothesis

3.1.1. Challenge

The strength of Al-Si piston alloys is influenced by the 3D architecture of Si and intermetallics. High service temperatures of modern combustion engines and heat treatments can lead to the coarsening of precipitates as well as to the spheroidization of Si and dissolution of intermetallics and thus, to a decrease of the interconnectivity which is essential for retaining high temperature strength. A crucial factor for the further development of these alloys lies in finding an appropriate compromise between sufficient ductility at RT, while retaining the highest possible strength at elevated temperatures. Even though the effect of 3D architecture (especially connectivity) on strength of cast Al-Si alloys has been subject to numerous investigations in recent years, the correlation between damage behavior and 3D connectivity of phases has received much less attention and has yet to be fully understood. Until now, the process and sequence of damage initiation and accumulation under external loads relevant for service conditions have mostly only been studied by 2D techniques. Owing to the advance of modern characterisation methods that allow observing the evolution of the microstructure in-situ and/or three-dimensionally, new insights on this crucial topic can be gained.

3.1.2. Aim and objectives

The capability of alloys to withstand external thermo-mechanical loads is determined by the mechanical and physical properties of the microstructural constituents, their thermal/mechanical stability and their geometrical arrangement (volume fraction, size, morphology, distribution, interconnectivity, contiguity). Intermetallic phases, formed by thermally stable alloying elements such as Cu, Ni, Mg and Fe, can contribute to the enhancement of the high temperature strength of cast Al-Si alloys by bearing mechanical loads.

In the present thesis, this is investigated in the frame of the following hypotheses:

1. Variations in chemical composition and thermal treatments can affect the architecture of the 3D interpenetrating network formed by Si and aluminides in cast Al-Si alloys.

2. The damage mechanisms during ambient and elevated temperature tensile deformation and the sequences of initiation and accumulation of damage can be fully revealed and analysed using in-situ 3D imaging methods. Microstructural features provoking damage initiation and failure can be univocally identified and evaluated qualitatively and quantitatively.

3. There is a correlation between the 3D architecture and the load bearing capability of rigid phases in cast Al-Si alloys. Especially the amount of connecting branches within the highly interconnected 3D hybrid network formed by Si and aluminides, i.e. the local connectivity, affects strength as well as damage evolution during tensile deformation at ambient and elevated temperatures.

3.1.3. Methodology

These hypotheses were investigated with the implementation of state of the art ex-situ and in-situ 3D imaging methods (XCT, sXCT) complemented by conventional 2D metallography investigations. This allows to reveal the internal architecture of the alloys and to monitor in-situ the formation and evolution of damage. The effect of microstructural features and test conditions on damage behaviour and also the sequence of damage mechanisms were determined. Room and high temperature in-situ tensile tests were conducted and their results were correlated with the 3D microstructure of Al-Si alloys as a function of alloy composition and heat treatment.

The obtained results and discussion of this research are presented as a collection of three articles published in peer-reviewed journals, which make up the basis of this Ph.D. thesis. K. Bugelnig planned and performed the experiments, analyzed the data, while she was also in charge of interpretation and discussion of results, and wrote the papers in close collaboration with G. Requena.

3.2.   Summary of published results

<u>I - Influence of 3D connectivity of rigid phases on damage evolution during tensile deformation of an AlSi12Cu4Ni2 piston alloy</u>

Materials Science and Engineering A 709 (2018), 193-202.
<u>Authors:</u> K. Bugelnig, F. Sket, H. Germann, T. Steffens, R. Koos, F. Wilde, E. Boller, G. Requena.

The 3D microstructural evolution of a cast AlSi12Cu4Ni2 piston alloy during solution treatment (ST) was identified and quantified. The microstructural changes were correlated with the process of damage formation and accumulation during tensile deformation at room temperature (RT). Ex-situ and in-situ synchrotron tomography as well as conventional metallography were combined to analyse microstructural evolution and damage evolution as a function of ST condition.

ST at 500°C for 4h provokes partial dissolution and morphological transformation of the Al_2Cu phase from blocky into coral-like structures. Also, slight spheroidization and fragmentation of eutectic and primary Si was observed. These changes result in a loss of connecting branches, i.e. loss of *local connectivity* (quantified by the Euler number χ) while matrix hardness and *global interconnectivity* of the 3D hybrid network, formed by Si and intermetallics, remain practically unaffected by the solution treatment.

The alloy in both conditions (as cast and 500°C/4h) shows that damage during RT tensile deformation occurs as a mixture of micro-cracks through primary Si particles agglomerated in clusters and occasional decohesion at the Si/Al-matrix interfaces. Coalescence of voids leads to final failure, with the main crack propagating exclusively along micro-cracks and rigid phases. Owing to the reduced local connectivity of the solution treated alloy, the alloy in this condition is capable of accommodating larger amounts of damage and plastic strain inducing an increase of ductility compared to the as cast condition.

The loss of local connectivity during solution treatment provokes a loss of load bearing capability of the 3D hybrid networks, thus decreasing strength and increasing ductility of the alloy in 4h ST condition compared to the as cast alloy.

II - Revealing the effect of local connectivity of rigid phases during deformation at high temperature of cast AlSi12Cu4Ni(2,3)Mg alloys

Authors: K. Bugelnig, H. Germann, T. Steffens, F. Sket, J. Adrien, E. Maire, E. Boller, G. Requena.

The microstructure of cast AlSi12Cu4Ni(2,3)Mg alloys and its effect on damage during tensile deformation at 300°C was investigated by 2D metallography and in-situ sXCT experiments.

An increase of Ni-content from 2 to 3 wt.% promotes the formation of the needle-like Al_3CuNi (δ-phase) which attributes to a significant increase in *local connectivity* by ~ 40% (quantified by the Euler number χ) at practically unchanged *global interconnectivity* (~ 95 %) of the 3D hybrid networks.

At 300°C, AlSi12Cu4Ni2Mg exhibits ~ 10% higher strength and ~ 30 % larger elongation at fracture compared to AlSi12Cu4Ni3Mg. For both alloys, damage forms in shape of micro-cracks through primary Si clusters as well as voids at matrix/rigid phase interfaces and in the matrix. Contrarily to RT observations, the main crack not only propagates along micro-cracks at rigid phases, but also through the Al-matrix. While the lower local connectivity of the hybrid network in the 2 wt.% Ni alloy allows for the accumulation of larger amounts of plastic strain in the matrix and damage prior to failure, the higher rigidity of the network in the 3 wt.% Ni alloy results in damage onset and failure at lower strains.

A simple load partition model based on sXCT data acquired during in-situ tensile tests was established, considering the continuous changes in local connectivity of the rigid networks with damage accumulation. Based on this model, the following conclusions are drawn:

(1) the lower local connectivity of the rigid networks in AlSi12Cu4Ni2Mg permits local plastification and strain hardening of the α-Al matrix resulting in the higher strength at 300°C compared to AlSi12Cu4Ni3Mg.

(2) the lower local connectivity of the rigid networks in AlSi12Cu4Ni2Mg also allows for accommodation of larger amounts of damage prior to failure resulting in the higher ductility of AlSi12Cu4Ni2Mg

III - Optimized segmentation of the 3D microstructure within cast Al-Si piston alloys

Authors: K. Bugelnig, H. Germann, T. Steffens, B. Plank, F. Wilde, E. Boller, G. Requena.

Even with the phase contrast provided by sXCT, an automatic segmentation of Si particles over a large volume is still problematic by simple global grey value thresholding. Analyzing the presence or absence of connecting branches, i.e. *local connectivity* of the 3D hybrid network of Si and aluminides in the magnitudes of only a few microns is essential for the full understanding of the thermo-mechanical behavior of cast near eutectic Al-Si alloys (see articles I + II). An optimized segmentation method with emphasis on a more accurate and automatic evaluation of local connectivity over large, representative volumes was developed. The 3D microstructure taking into account all microstructural constituents has been characterized by means of combined x-ray tomography, synchrotron tomography and chemical deep etching + tomography.

A quantitative and qualitative comparison between results of the conventional semi-automatic and the optimized segmentation method reveals that the results of the quantification are strongly influenced by the accuracy of the segmentation method. The optimized method provides a more realistic representation of Si-aluminide interfaces and thus, a more accurate consideration of local connectivity of the 3D hybrid network is made possible. Furthermore, a crucial improvement is the automatic segmentation of all microstructural constituents by simple global grey value thresholding. This provides a more accurate evaluation of all the phases present within the material and their interaction with each other (e.g. local connectivity) over large, representative volumes.

Chapter 4

CONCLUSIONS

The aim of this work was the identification of microstructural features affecting damage formation, damage accumulation and sequence of occurring damage mechanisms during tensile deformation at ambient and elevated temperatures in cast Al-Si piston alloys. A quantitative relationship between 3D architecture of the investigated alloys and microstructural features affecting damage processes during external loading could be univocally established. Besides the specific conclusions given in the three peer-reviewed publications, the following general conclusions can be drawn.

1. <u>Tomography data processing (article III)</u>

A combination of different 3D imaging methods (XCT, sXCT, chemical deep etching + tomography) was utilized to develop an optimized segmentation method focusing on more accurate evaluation of *local connectivity* over large, representative volumes. This method allows avoiding the problem of local contrast variations owing to the presence of highly absorbing intermetallic phases neighboring Si particles and phase contrast artefacts at aluminide/Al-matrix interfaces. Image segmentation of all microstructural constituents within the material can thus be achieved in large volumes by simple global grey value thresholding. The results may be used as ground truth segmentation for training deep learning algorithms that can produce fully automatic segmentation of the 3D architecture of this type of alloys.

2. <u>Correlation between 3D microstructure, damage and strength (articles I & II)</u>

The topological parameter Euler number has proven to be a useful tool for characterizing *local connectivity*, providing information about the 3D architecture of cast Al-Si alloys.

It has been demonstrated that, for the investigated alloys, variations in applied solution treatment (0h/500°C vs 4h/500°C) and alloy composition (2 wt.% Ni vs 3 wt.% Ni) primarily result in a change of local connectivity of the 3D interpenetrating networks of Si and aluminides, while other parameters such as volume fraction, global

interconnectivity of rigid phase networks and matrix hardness remain practically constant.

In-situ synchrotron tomography during tensile testing allowed to monitor and analyze damage mechanisms and their sequence of occurrence. Damage mechanisms during ambient and elevated temperature tensile deformation were identified to be strongly associated with primary Si particles grouped in clusters.

Furthermore, a correlation between strength, elongation at fracture and local connectivity of rigid phases could be determined. While parameters usually associated to damage remain unchanged for the different alloys and alloy conditions studied (volume fraction and global interconnectivity of rigid phases), it is revealed that the degree of branching within the 3D hybrid networks formed by Si and intermetallic phases, i.e. the local connectivity (quantified by Euler number χ), poses the main factor responsible for differences in tensile behavior and damage evolution during tensile deformation at RT and 300°C. Even though a change in local connectivity of the hybrid network (by ~ 40%) does not seem to affect the types of damage mechanisms regardless of test temperature, the amount of damage accumulated prior to failure increases (by ~ 55% and ~ 66% at RT and 300°C, respectively), while damage at the same applied strain decreases with decreasing local connectivity. At RT, 40% lower local connectivity results in a decrease in strength (by 8 %) while elongation at fracture increases by 44 %. At 300°C, the lower local connectivity allows for the accommodation of larger amounts of plastic strain in the matrix and thus, additional strain hardening leads to 10% higher tensile strength, while the elongation at fracture increases by 30% owing to the larger amount of damage accumulated compared to the alloy with 40% higher local connectivity.

The integration of 3D data acquired experimentally into load partition models gives further insight on the effect of damage on strength in cast Al-Si alloys, successfully allowing to rationalize the effect of global interconnectivity and local connectivity.

Chapter 5

FUTURE DIRECTIONS

In the course of this thesis, several challenges, which still need further investigation, came to light:

Alloy design

Further consideration should be given to the composition of intermetallic phases to determine the role of alloying elements such as Fe or Mn as well as the effect of specific ratios of Ni/Cu, Ni/Fe or Cu/Mg which could provide more thermal and mechanical stability to the 3D hybrid network. This could be investigated theoretically using thermodynamic calculations combined with high resolution 3D elemental sensitive imaging.

Furthermore, this work revealed the significant role that clusters of primary Si particles play regarding damage formation and accumulation in near eutectic Al-Si alloys. It is recommended to further investigate ways to reduce the size and inhomogeneous distribution of primary Si to retard damage formation. Possible routes would be Sr modification or further reduction of Si content. However, the effect of these measures on castability, machinability and wear resistance requires further investigation.

Experimental methods

The in-situ sXCT data should be complemented by in-situ bulk diffraction methods to get insights on the load-carrying capability and load partition of 3D reinforcing structures.

Data processing

At present, the characterization of all microstructural constituents in cast Al-Si alloys in large tomographic volumes is associated with very time-consuming segmentation methods. It is highly recommended to introduce machine learning/deep learning approaches to increase time-efficiency as well as accuracy and representativity during image segmentation.

Implementation of experimental data into finite element models

The voxel-based tomography datasets are well suited for the combination with simulation tools. In the frame of this work, first modelling approaches considering the correlation between the load bearing capability of the rigid phases and Al-matrix, and the local connectivity of the 3D hybrid networks, were established. In a next step, physical models based on the experimental observations (tomographic and diffraction data) should be implemented into simulation tools. The creation of representative 3D finite element models for the simulation and rationalization of the damage evolution during thermo-mechanical loading is of high interest.

[1]   The European Parliament and the Council of the European Union, Directive 2000/53/EC of the European Parliament and of the Council of 18 September 2000 on End-of-Life Vehicles (2000), 34-42.

[2]   S. Spangenberg, T. Hettich, M. Lazzara, K. Scherer, 35. Internationales Wiener Motorensymposium (2014), 204-216.

[3]   H. Germann (KS. Kolbenschmidt GmbH), Werkstoffkundliches Kolloquium, TU Kaiserslautern (2014).

[4]   F.S. Silva, Engineering Failure Analysis 13 (2006), 480-492.

[5]   G. Floweday, S. Petrov, R.B. Tait, J. Press, Engineering Failure Analysis 18 (2014), 1664-1674.

[6]   M. Javidani, D. Larouche, International Meterials Reviews 59 (3) (2014), 132-158.

[7]   KS Kolbenschmidt GmbH, Innovative Kolbentechnologie für Pkw und Nkw von KS Kolbenschmidt: Systemkompetenz rund um den Kolben (2013).

[8]   J.R. Davies, ASM Special Handbook: Aluminium and aluminium alloys, ASM international (1993), ISBN: 978-0-87170-496-2.

[9]   L. Tian, Y. Guo, J. Li, F. Xia, M. Liang, Y. Bai, Materials 11 (2018), 1230.

[10]   K. Morimoto, H. Takamiya, Y. Awano, M. Nakamura, Journal of Japan Institute of light Metals 38 (1988), 779-783.

[11]   J. Jorstad, D. Apelian, International Journal of Metalcasting (2009), 14-36.

[12]   L.F. Mondolfo, Aluminum Alloys: Structures and Properties, Butterworth &Co (Publishers) Ltd (1976), ISBN 0 408 70932 4.

[13]   G. Requena, H. P. Degischer, Annual Review of Materials Research 42 (2012), 151-161.

[14]   Z. Asghar, G. Requena, E. Boller, Acta Materialia 59 (2011), 6420-6432.

[15]   G. Requena, G. Garcés, Z. Asghar, E. Marks, P. Staron, P. Cloetens, Advanced Engineering Materials 13 (2011), 674-684.

[16]   M. Zamani, Al-Si Cast Alloys – Microstructure and Mechanical Properties at Ambient and Elevated Temperature, Ph.D. Thesis, Jönköping University, Sweden, March (2015).

[17]   S.G. Shabestari, H. Moemeni, Journal of Materials Processing Technology 153-154 (2004), 193-198.

[18]   F. Lasagni, A. Lasagni, E. Marks, C. Holzapfel, F. Mücklich, H. P. Degischer, Acta Materialia 55(11) (2007) 3875–3882.

[19]   M. Zamani, S. Seifeddine, M. Azuzuderourei, Light Metals 2013, ed. B. Sadler, TMS (2013), 297-302.

[20]   M.M. Makhlouf, H.V. Guthy, Journal of Light Metals 1(4) (2001), 199-218.

[21]   S.-Z. Lu, A. Hellawell, Metall. Trans. A. 18 (1987) 1721–1733.

[22]   H. A. Elhadari, H. A. Patel, D. L. Chen, W. Kasprzak, Mater. Sci. Eng. A 528(28) (2011), 8128–8138.

[23]   H.B. Nadendlai, M. Nowaki, L. Bolzoni, Light Metals 2013, Barry Sadler (Ed.), TMS (2013), 1009.

[24]   S. Hegde, K.N. Prabhu, Journal of Materials Science 43 (2008), 3009–3027.

[25]   K.F. Kobayashi, L.M. Hogan, Journal of Materials Science 20 (1985), 1961–1975.

[26]   S.A. Alkahtani, E.M. Elgallad, M.M. Tash, A.M. Samuel, F.H. Samuel, Materials 9 (2016), 45.

[27]   C.L. Chen, A. Richter, R.C. Thomson, Intermetallics 18(4) (2010), 499–508.

[28]   R. Wang, W. Lu, L.M. Hogan, Journal of Crystal growth 207 (1999), 43-54.

[29]   J. Wang, Z. Guo, J.L. Song, W.X. Hu, J.C. Li, S.M. Xiong, Scientific Reports 7 (2017), 14994.

[30]   J. Wang, Z. Guo, J.L. Song, W.X. Hu, J.C. Li, S.M. Xiong, Materials and Design 137 (2018), 176-183.

[31]   W. Edwards, Microstructural and mechanical property modelling for the processing of Al-Si alloys, Ph.D. Thesis, Loughborough University (2002).

[32]   L. Yu, X. Liu, H. Ding, X. Bian, Journal of Alloys and Compounds 432 (2007), 156-162.

[33]   J. Li, F.S. Hage, Q. Ramasse, P. Shumacher, Scientific Reports 6 (2016), 25244.

[34]   G. Singworth, J. Campell, J. Jorstad, International Journal of metalcasting 3(1) (2009), 65-78.

[35]   G.C. Requena, P. Degischer, E.D. Marks, E. Boller, Materials Science and Engineering A 487 (2008), 99-107.

[36]   Z. Asghar, G. Requena, Materials Science and Engineering A 591 (2014), 136-143.

[37]   D.Tolnai, G. Requena, P. Cloetens, J. Lendvai, H.P. Degischer, Materials Science and Engineering A 585 (2013), 480-487.

[38]   J.-G. Jung, S.-H. Lee, J.-M. Lee, Y.-H. Cho, S.-H. Kim, W.-H. Yoon, Materials Science & Engineering A 669 (2016), 187–195.

[39]   Z. Asghar, G. Requena, F. Sket. Journal of Microscopy (2015), 1-9.

[40]   N. A. Belov, D. G. Eskin, and N. N. Avxentieva, Acta Mater. 53(17) (2005), 4709–4722.

[41]   A.R. Farkoosh, M. Javidani, M. Hoseini, D. Larouche, M. Pekguleryuz, Journal of Alloys and Compounds 551 (2013), 596-606.

[42]   Y. Liu, F. Meirer, J. Wang, G. Requena, P. Williams, J. Nelson, A. Mehta, J.C. Andrews, P. Pianetta, Analytical and Bioanalytical Chemistry 404 (2012), 1297–1301.

[43]   A.M.A. Mohamed, F.H. Samuel, INTECH (2012), 56-72.

[44]   M. A. Moustafa, F.H. Samuel, H.W. Doty, Journal of Materials Science 38 (2003), 4507-4522.

[45]   P.Y. Zhu, Q.Y. Liu, T.X. Hou, AFS Transactions 93 (1985), 609-614.

[46]   Y. Han, A.M. Samuel, H.W. Doty, S. Valtierra, F.H. Samuel, Materials and Design 58 (2014), 426-438.

[47]   G. Requena, G. Garcés, M. Rodrßigues, T. Pirling, P. Cloetens, Advanced Engineering Materials 11 (2009), 1007-1014.

[48]   R. Koos, Correlation between 3D microstructure and thermo-mechanical behavior of near eutectic piston alloys, Ph.D. Thesis, TU Vienna, November (2014).

[49]   Z. Asghar, G. Requena, E. Boller, Acta Materialia 59 (2011), 6420–6432.

[50]   H. Röhrig, E. Käpernick, Aluminium 23 (1941), 235-239.

[51]   F. Paray, J.F. Gruzleski, Cast Metals 7 (1994), 29–40.

[52]   Z. Asghar, G.Requena, H.P. Degischer, P. Cloetens, Acta Materialia 57 (2009), 4125-4132.

[53]   Z. Asghar, G. Requena, F. Kubel, Mater. Sci. Eng. A 527(21–22) (2010), 5691–5698.

[54]   C.H. Cáceres, M.B. Djurdjevic, T.J. Stockwell, J.H. Sokolowski, Scripta Materialia 40 (1999), 631-637.

[55]   H. Ye, Journal of Materials Engineering and Performance 12(3) (2003), 288-297.

[56]   M. Kobayashi, Y. Dorce, H. Toda, H. Horikawa, Materials Science and Technology. 26 (2010), 962-967.

[57]   T.O. Mbuya, P.A.S. Reed, Materials Science and Engineering A 612 (2014), 302-309.

[58]   A.J. Moffat, B.G. Mellor, C.L. Chen, R.C. Thomson, P.A.S. Reed, Materials Science Forum 519–521 (2006) ,1083–1088.

[59]   R. Konečná, G. Nicoletto, L. Kunz, M. Svoboda, and A. Bača, Procedia Eng. 74 (2014), 43–46.

[60]   F. Stadler, H. Antrekowitsch, W. Fragner, H. Kaufmann, P.J. Uggowitzer, International Journal of Cast Metals Research 25(4) (2012), 215-224.

[61]   K.E. Knipling, D.C. Dunnand, D.N. Seidman, Z. Metallkd. 97(3) (2006), 246-265.

[62]   K.E. Knipling, D.C. Dunand, D.N. Seidman, Acta Materialia 56 (2008), 114-127.

[63]   J. Rakhmonov, G Timelli, F. Bonollo, Advanced Engineering Materials 18(7) (2016), 1096-1105.

[64]   K. E. Knipling, D. C. Dunand, D. N. Seidman, Acta Materialia 56 (2008), 1182-1195.

[65]   T. Ohashi, R. Ichikawa., Metallurgical Transactions 3(8) (1972), 2300-2302.

[66]   Y. Zhang, W. Zhou, H. Gao, Y. Han, K. Wang, J. Wang, Scripta Materialia 69(6) (2013), 477-480.

[67]   C. Booth-Morrison, D.N. Seidman, D.C. Dunand, Acta Materialia 60(8) (2012), 3643-3654.

[68]   J.G. Kaufman, E.L. Rooy, Aluminum Alloy Castings: Properties, Processes, and Applications, ASM International (2004), ISBN: 0-87170-803-5.

[69]   H. Yang, S. Ji, W. Yang, Y. Wang, Z. Fan, Materials Science and Engineering A 642 (2015), 340-350.

[70]   E. Ogris, Development of Al-Si-Mg Alloys for Semi-solid processing and silicon spheroidization treatment (SST) for Al-Si cast alloys, Shaker Verlag Aachen (2002), ISBN 3-8322-0892-5.

[71]   Z. Wenda, Y. Jing, D. Jingzhi, L. Yun, X. Hong, Advanced Materials Research 652-654 (2013), 1030-1034.

[72]   F.A. Lasagni, The Role of Si on the Microstructure of Al Casting Alloys and Short Fibre Composites, Shaler Verlag GmbH, Germany, (2008), ISBN: 9783832268336.

[73]   D. Hull, T.W. Clyne, An introduction to composite materials (Cambridge Solid State Science Series) 2nd edition, Cambridge university press (1996), ISBN: 0-521-38190-8.

[74]   M. Zamani, S. Seifeddine, A.E.W. Jarfors, Materials and Design 86(5) (2015), 361-370.

[75]   C. Otto, Neuer Aluminium-Kolben für Hochleistungs-Dieselmotoren, Automobil-Industrie, 20.6.2012.

[76]   D.K. Dwividi, R. Sharma, A. Kumar, International Journal of Cast Metals Research 19 (2006), 275-282.

[77]   Y. Wang, H. Liao, Y. Wu, J. Wang, Materials and Design 53 (2014), 634-638.

[78]   H. Elzanaty, Impact: International Journal of Research in Engineering & Technology 2 (2014), 49-54.

[79]   M.D. Dighe, A.M. Gokhale, Scripta Materialia 37 (1997) 1435–1440.

[80]   H. Liao, Y.Sum, G. Sun, Materials Science and Engineering A 335 (2001), 62-65.

[81]   M. Zamani, S. Seifeddine, A.E.W. Jarfors, Proceedings to TMS (The Materials, Metals & Materials Society), San Diego, USA (2014).

[82]   M.G. Mueller, M. Fornabaio, G. Zagar, A. Mortensen, Acta Materialia 105 (2016), 165-175.

[83]   M. R. Joyce, C. M. Styles, and P. A. S. Reed, Int. J. Fatigue 25(9–11) (2003), 863–869.

[84]   A. Gangulee, J. Gurland, Transactions of the Metallurgical Society of AIME, 239(2) (1967), 269-272.

[85]   K. Gall, M. Horstemeyer, D. L. McDowell, J. Fan, Mech. Mater. 32(5) (2000), 277–301.

[86]   S. Joseph, S. Kumar, Materials Science and Engineering A 588 (2013), 11-124.

[87]   P.K. Rohatgi, R.C. Sharma, Prabhakar, American Society for Metals, The Melallurgical Society of AIME 6 (1975), 569.

[88]   J.A. García-Hinojosa, C.R. González, G.M. González, Y. Houbaert, Journals of Materials and processing technology 143 (2003); 306-310.

[89]   M.A. Moustafa, F.H. Samuel, H.W. Doty, Journal of Materials Science 38 (2003) 4523-4534.

[90]   E.R. Wang, X.D. Hui, S.S. Wang, Y.F. Zaho, G.L. Chen, Materials Science and Engineering A 527 (2010), 7878.

[91]   S. Hukai, K. Takeuchi, E. Tanaka, Journal of the Society of Materials Science Japan 13(126) (1964), 190-196.

[92]   Y.H. Cho, Y.R. Im, S.W. Kwon, H.C. Lee, Materials Science Forum 426-432 (2003), 339-344.

[93]   L. Yunguo, Y. Yang, Y. Wu, L. Wang, X. Liu, Materials Science and Engineering A 527 (2010), 7132-7137.

[94]   A.J. Moffat, B.G. Mellor, I. Sinclair, P.A.S. Reed, Materials Science and Technology 23(12) (2007), 1396-1401.

[95]   M. Schöbel, G. Baumgartner, S. Gerth, J. Bernardi, M. Hofmann, Acta Materialia, 81 (2014), 401-408.

[96]   A. Couture, AFS International Cast Metals Journal 6 (1981), 9-17.

[97]   P.N. Crepeau, ASF Transactions 103 (1996), 361-366.

[98]   J.A. Taylor, Proceedings to 35th Australian Foundry Institute National Conference, Australian Foundry Institute (AFI), Adelaine, South Australia (2004), 148-157.

[99]   G. Zhang, J. Zhang, B. Li, W. Cai, Progress in Natural Science: Materials International 21 (2011), 380-385.

[100] A. Tireira, G. Requena, S. Sao Jao, A. Borbely, H. Klocker, Acta Materialia 112 (2016), 162-170.

[101] M. Sahoo, R. Smith, Metal Science 9 (1975), 217-222.

[102] Z. Asghar, G. Requena, G.H. Zahid, Rafi-ud-Din, Materials Characterization 88 (2014), 80-85.

[103] D.B. Aydogan, J. Hyttinen, the Royal Society Interface 11 (2014), 1-10.

[104] J. Toriwaki and T. Yonekura, Forma 17(3) (2002), 183–209.

[105] A. Odgaard, H.J.G. Gundersen, Bone. 14 (1993), 173–182.

[106] M.J. Silva, L.J.Gibson, International Journal of Mech.Sci. 39(5) (1997), 549-563.

[107] A. Kruglova, M. Engstler, G. Gaiselmann, O. Stenzel, V. Schmidt, M. Roland, S. Diebels, F. Mücklich, Computational Material Science 120 (2016), 90-107.

[108] R.W. Hamilton, D. See, S. Butler, P.D. Lee, Materials Science and Engineering A 343 (2003), 290-300.

[109]   M. Suéry, J. Adrien, C. Landron, S. Terzi, E. Maire, L. Salvo, J.-J. Blandin, International Journal of Materials Research 101(9) (2010), 1080-1088.

[110]   K.H. Khor, J.Y. Buffière, W. Ludwig, H. Toda, H.S. Ubhi, P.J. Gregson, I. Sinclair, Journal of Physics Condensed Matter 16 (2004), 3511-3515.

[111]   J. Kastner, B. Harrer, H.P. Degischer, Materials Characterization (2011), 99-107.

[112]   L. Salvo, P. Cloetens, E. Maire, S. Zabler, J.J. Blandin, J.Y. Buffière, W. Ludwig, E. Boller, D. Bellet, C. Josserond, Instruments Methods Phys. Res. Sect. B Beam Interact. with Mater. Atoms 200 (2003), 273-286.

[113]   J. Banhart, Advanced Tomographic Methods in Materials Research and Engineering, Oxford University Press 2008, ISBN 978-0-19-921324-5.

[114]   B. Harrer and J. Kastner (Book chapter), in: F. A. Lasagni, A. F. Lasagni (editors), New Trends for two and three Dimensional Structures 10, Springer Verlag, Berlin Heidelberg (2011), 119-150.

[115]   T. M. Buzug, Introduction to Computed Tomography: From Photon Statistics to Modern Cone-beam CT, Springer (2008), ISBN: 978-3-540-39407-5.

[116]   D. Tolnai, G. Requena, P. Cloetens, J. Lendvai, H.P. Degischer, Materials Science and Engineering A 550 (2012), 214-221.

[117]   G. Requena, P. Cloetens, W. Altendorfer, C. Poletti, D. Tolnai, F. Warchomicka,. Scripta Materialia 61 (2009), 760- 763.

[118]   A. Borbély, P. Cloetens, E. Maire, G. Requena, In Fabrication and Characterization in the Micro-Nano Range. In FA Lasagni, AF Lasagni(Eds), Springer, Berlin (2011), 151-170.

[119]   S.C. Wu, T.Q. Xiao, Engineering Mechanics 182 (2017), 127-156.

[120]   E. Maire, P.J. Withers, International Materials Reviews 59(1) (2014), 1-43.

[121]   W. Ludwig, A. King, M. Herbig, P. Reischig, J.T. Marrow, L. Babout, E.M. Lauridsen, H. Proudhon, J.Y. Buffiere, JOM Journal of the Minerals, Metals and Materials Society, Springer Verlag (Germany) (2010), 22-28.

[122]   P. Staron, A. Schreyer, H. Clemens, S. Mayer, Neutrons and Synchrotron Radiation in Engineering Materials Science: From Fundamentals to Applications, Second Edition, Wiley-VCH Verlag GmbH & Co. KGaA (2017), ISBN: 9783527335923.

[123]   D. Paganin, S.C. Mayo, T.E. Gureyev, P.R. Miller, S.W. Wilkins, Journal of Microscopy 2016 (2002); 33–40.

[124]   T. Weitkamp, D. Haas, D. Wegrzynek, A. Rack, Journal of Synchrotron Raiation 18. (2011), 617-629.

[125]   L. Salvo, M. Suéry, A. Marmottant, N. Limodin, D. Bernard, Comptes Rendus Physique 11 (2010), 641-649.

[126]   P. Cloetens, R. Barrett, J. Baruchel, J. P. Guigay, M. Schlenker, Journal of Physics D: Applied Physics 29 (1996), 133-146.

[127]   S.C. Mayo, A. Stevenson, S.W. Wilkins, Materials 5 (2012), 937-965.

[128]   P. Cloetens, W. Ludwig, J. Baruchel, D. Van Dyck, J. Van Landuyt, J. P. Guigay, M. Schlenker, Applied Physics Letters 75(19) (1999), 2912–2914.

[129]   P. Lhuissier, M. Scheel, L. Salvo, M. Di Michiel, J.J. Blandin, Scripta Materialia 69 (2013), 85–88.

[130]   J.Y. Buffière, E. Maire, J. Adrien, J.P. Masse, E. Boller, Experimental Mechanics 50 (2010), 289-305.

[131]   H. Zhang, H. Toda, P.C. Qu, Y. Sakaguchi, M. Kobayashi, K. Uesugi, Y. Suzuki, Acta Materialia 57 (2009), 3287-3300.

[132]   E. Ferrie, J.Y. Buffière, W. Ludwig, International Journal of Fatigue 27 (2005), 1215-1220.

[133]   J. J. Gammage, D. S. Wilkinson, J. D. Embury, E. Maire, Philos. Mag. 85(26–27) (2005), 3191–3206.

[134]   L. Babout, E. Maire, R. Fougères, Acta Materialia 52 (2004), 2475-2487.

[135]   J. Y. Buffière, E. Maire, P. Cloetens, G. Lormand, R. Fougères, Acta Materialia 47(5) (1999), 1613–1625.

[136]   L. Babout, W. Ludwig, E. Maire, J.Y. Buffiere, Nucl. Instruments Methods Phys. Res. Sect. B Beam Interact. with Mater. Atoms 200 (2003), 303–307.

[137]   E. Maire, S. Zhou, J. Adrien, M. Dimichiel, Eng. Fract. Mech. 78(15) (2011), 2679–2690.

[138]   F. Wilde, M. Ogurreck, I. Greving1, J. U. Hammel, F. Beckmann, A. Hipp, L. Lottermoser, I. Khokhriakov, P. Lytaev, T. Dose, H. Burmester, M. Müller, A. Schreyer, AIP Conference Proceedings 1741 (2016), 030035.

[139]   http://www.esrf.eu/home/UsersAndScience/Experiments/StructMaterials

/ID19.html

Appendix A

PUBLICATIONS

K. Bugelnig, F. Sket, H. Germann, T. Steffens, R. Koos, F. Wilde, E. Boller, G. Requena*; Influence of 3D connectivity of rigid phases on damage evolution during tensile deformation of an AlSi12Cu4Ni2 piston alloy*, Materials Science and Engineering A 709 (2018), 193-202. DOI: 10.1016/j.msea.2017.10.035.

K. Bugelnig, H. Germann, T. Steffens, F. Sket, J. Adrien, E. Maire, E. Boller, G. Requena*; Revealing the Effect of Local Connectivity of Rigid Phases during Deformation at High Temperature of Cast AlSi12Cu4Ni(2,3)Mg Alloys*, Materials 11 (2018), 1300.

K. Bugelnig, H. Germann, T. Steffens, B. Plank, F. Wilde, E. Boller, G. Requena*; Optimized Segmentation of the 3D Microstructure in Cast Al-Si Piston Alloys*, Practical Metallography 55(4) (2018), 223-243.